

Population genetics in microchannels

Anzhelika Koldaeva¹, Hsieh-Fu Tsai², Amy Q. Shen², and Simone Pigolotti^{1*}

¹*Biological Complexity Unit, Okinawa Institute for Science and Technology
and Graduate University, Onna, Okinawa 904-0495, Japan and*

²*Micro/Bio/Nanofluidics Unit, Okinawa Institute for Science and
Technology and Graduate University, Onna, Okinawa 904-0495, Japan*

(Dated: May 29, 2022)

Spatial constraints such as rigid barriers affect the dynamics of cell populations, potentially altering the course of natural evolution. In this paper, we study the population genetics of *Escherichia coli* proliferating in microchannels with open ends. Our experiments reveal that competition among two fluorescently labeled *E. coli* strains growing in a microchannel generates a stripe pattern aligned with the axial direction of the channel. To account for this observation, we study a lattice population model in which reproducing cells push entire lanes of cells towards the open ends of the channel. By combining mathematical theory, numerical simulations, and experiments, we find that the fixation dynamics is extremely fast along the axial direction, with a logarithmic dependence on the number of cells per lane. In contrast, competition among lanes is a much slower process. We also demonstrate that random mutations that appear in the middle and at the boundaries of the channel are highly likely to reach fixation. By theoretically studying competition between strains of different fitness, we find that the population structure in such a spatially confined system strongly suppresses selection.

I. INTRODUCTION

Biological populations can be spatially organized by landscape barriers that constrain individual movement, potentially generating ordered patterns at the population level. For example, populations of rod-shaped bacteria *Escherichia coli* growing on surfaces tend to organize into domains of aligned cells [1, 2]. When *E. coli* grows in confined channels, cell alignment is affected by the geometry of the channel boundaries [3, 4]. In narrow channels, populations reach a highly ordered structure, with cells parallel to each other and to the boundaries [5, 6]. In wide channels, this alignment is disrupted at large scales by a buckling instability [7].

Population growth in confined geometries is common in nature. For instance, bacteria commonly proliferate in porous media such as soil, where fluid flows supply cells with nutrients [8]. Epithelial tissues in multicellular organisms present a similar spatial organization. They consist of multiple compartments of cells that originates at a stem cell layer [9]. These stem cells divide and generate differentiated cells that are pushed toward the top of the compartment. They can be eliminated from the tissue once they reach the surface. Such mechanism reduces the rate of accumulation of deleterious mutations, thereby decreasing the risk of cancer [10].

Microfluidic devices are convenient tools to experimentally study population growth in spatially confined geometries. They enable mimicking microorganism habitats by adjusting the size and shape of each microchannel and controlling the flows that supply microorganisms inside the channels with nutrients [11]. Such devices are often used to track population dynamics of microorganisms

at the single-cell level over several generations [12–14]. A paradigmatic example is the “mother machine” – a microchannel with one open end and small enough width to accommodate a single lane of cells [15]. Microchannels with two open ends have been used to validate the relation between the cell division time distribution and the growth rate of the whole population [16].

In all these examples, once the cell population densely fills an entire channel, dividing cells push others toward the open ends, potentially leading to expulsion of cells. The timescale at which cells are expelled is typically shorter than their lifetime. Therefore, death events can be usually neglected – cells do not compete for survival, but rather for remaining inside the channel. In genetically diverse populations, we expect such competition to cause diversity loss at a pace that depends on the channel geometry.

To study population genetics in small confined geometries, individual coordinates must be taken into account. There exists a vast literature on spatially-explicit individual-based models, ranging from Kimura’s stepping stone model [17, 18] to generalizations in the theory of evolutionary graphs [19–22]. However, the processes included in these models are usually limited to birth, death, and diffusion events, and do not account for the effect of cells pushing each other in a confined geometry. Microbial population dynamics incorporating this latter ingredient has been investigated with computational approaches [16, 25]. In particular, simulations of a model of competing bacterial strains [25] show a formation of lanes along the channel axial direction. Some aspects of pushing dynamics have been theoretically studied in the context of cancer progression [23, 24].

In this paper, we study the population genetics of bacterial colonies growing in confined geometries. We combine theory, numerical simulations, and experiments on

* simone.pigolotti@oist.jp

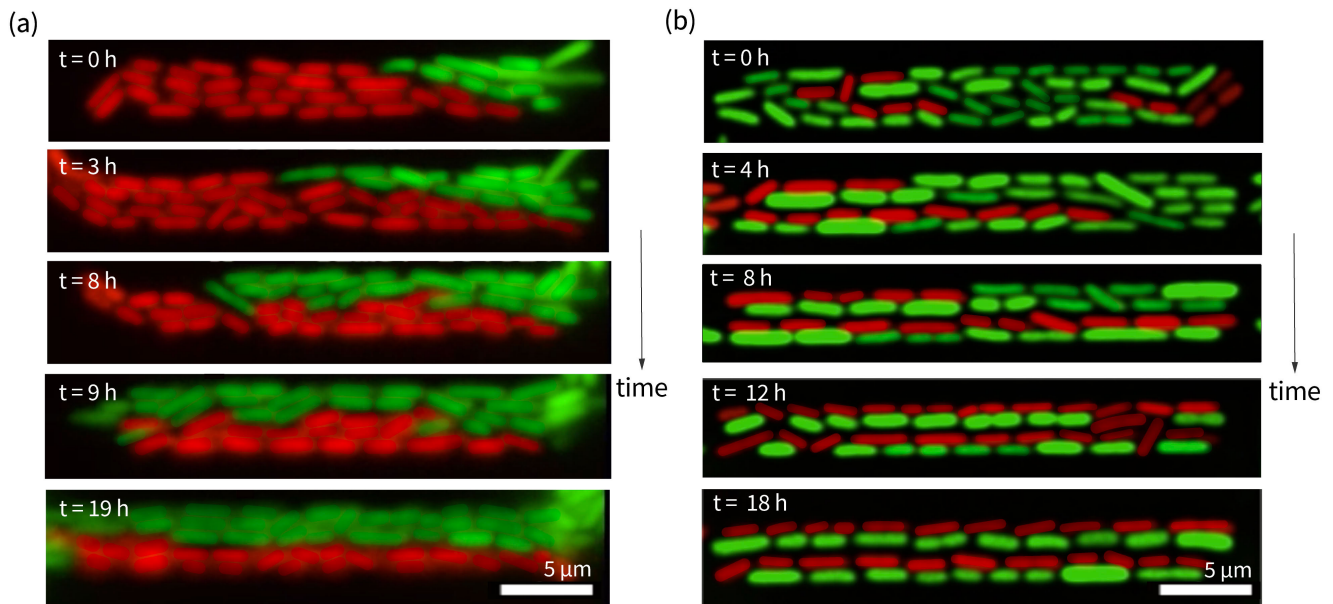


FIG. 1. Snapshots of two strains of *E. coli* competing in a microchannel with two open ends. The two panels show two independent realizations under the same experimental conditions. (a) Competing strains segregate into two stripes. (b) Competing strains segregate into four stripes.

E. coli populations growing in straight microchannels with two open ends. We first perform experiments with two competing neutral strains, colored with different fluorescent proteins. In these experiments, we observe formation of a stripe pattern aligned with the channel axial direction. To understand this phenomenon, we solve a lattice model analytically for the competition dynamics in each lane. The solution reveals that fixation of neutral strains within each lane is much faster than predicted by traditional spatial population genetics. We then extend this result to a model including multiple lanes by a combination of analytical methods and numerical simulations. Our model, validated by experimental results, shows that competition between lanes is much slower than competition within lanes. We finally consider competition in the presence of a mutant carrying a selective advantage. We find that selection in such a spatially confined geometry is much less effective than in well-mixed populations.

The paper is organized as follows. In Section II, we briefly introduce our experimental setup and present the stripe pattern that we observe in competing *E. coli* populations. In Section III, we introduce the basic version of our model and its main predictions. In Section IV, we generalize the model to include biases in the direction of reproduction events observed in experiments. In Section V, we study the loss of genetic diversity predicted by the model and compare it with experimental results. In Section VI we predict the fixation time. In Section VII, we extend our results to the mother machine. In Section VIII, we study fixation probabilities as a function of the cell position. In Section IX, we study the strength

of selection in a microchannel where a non-neutral mutation arises. Section X is devoted to conclusions and perspectives. Finally, Section XI provides details on our experimental, mathematical, and computational results.

II. *E. COLI* IN MICROCHANNELS

We conduct experiments with growing populations of *E. coli* in microfluidic devices that consists of multiple rectangular growth microchannels of same length but different widths. Both ends of each growth microchannel are open to flow channels. From now on, we refer to the growth microchannels simply as “microchannels”. Bacteria reproduce in nutrient-rich conditions inside the microchannels and push each other toward the open ends. As a result, cells are continuously expelled into the flow channels. Reproductions and expulsions balance each other in such a way that the number of cells inside the microchannels remains nearly constant. We record the evolution of the bacterial populations using time-lapse fluorescence microscopy with 3 min temporal resolution.

Due to the system geometry and the elongated shape of *E. coli*, bacteria tend to align and form lanes along the axial direction of the microchannels. Such lanes occupy the entire length of the microchannel and their number depends on the width of the microchannel, see supplementary video. We evaluate the number of lanes and their lengths from the experimental data, see Section IV A.

To directly observe competition inside the microchannels, we perform experiments with a mixture of two

strains of *E. coli* labeled with green and red fluorescent protein, see Fig. 1a, b and supplementary video. We observe that population dynamics tends to generate stripe patterns of the two strains. These stripes are aligned with the axial direction of the microchannels. Their number and width depends on the microchannel size and also varies depending on the initial conditions of the experiments.

To understand the origin of these patterns, we perform more extensive experiments with a single *E. coli* strain and track the descendants of each individual in the initial population, see Methods sections XI A and XI B. Our tracking algorithm classifies bacteria inside each microchannel into clonal populations, i.e. groups of individuals that descend from a common ancestor in the initial population. The dynamics of the clonal populations permits to determine the patterns that the population would develop if some of the clones were fluorescently marked, or carried a neutral mutation, i.e., a mutation that does not affect fitness.

III. MODEL WITH UNIFORM REPRODUCTION

We start our theoretical analysis with a simple lattice model in which probabilities of cells reproducing in different directions are uniform. This model has been proposed and numerically studied in [16, 25]. We first consider the case of a thin microchannel harboring a single lane of N cells, see Fig. 2a. Cells reproduce at a constant rate b . After reproduction, one of the daughter cells takes the position of its mother. The second one occupies the lattice site either to the left or right of the mother and pushes existing cells toward one open end of the microchannel depending on the direction of the reproduction. As a result, a cell at the open end is expelled from the microchannel. If a reproducing cell is located next to an open end, its daughter cell can end up outside the microchannel, thereby being immediately expelled. Such updating rules maintain the number of cells in the microchannel as a constant in time. Because of our assumption of uniform reproduction, the probabilities that the daughter occupies the lattice site to the left or to the right of the mother are both equal to $1/2$.

We call $A(t)$ the number of clonal populations at time t . At the initial time $t = 0$, the population is made up of $A(t = 0) = N$ clonal populations. This number progressively decreases with time, as progenies of initial individuals are expelled from the microchannel, see Fig. 2b. We study the dynamics of the clonal populations more deeply in the following.

The fixation time T_{fix} is the time at which one of the clonal populations has taken over the whole population. In the model with uniform reproduction, we find that the average fixation time is well approximated by

$$\langle T_{\text{fix}} \rangle \approx b^{-1} [\log(N - 1) + \gamma], \quad (1)$$

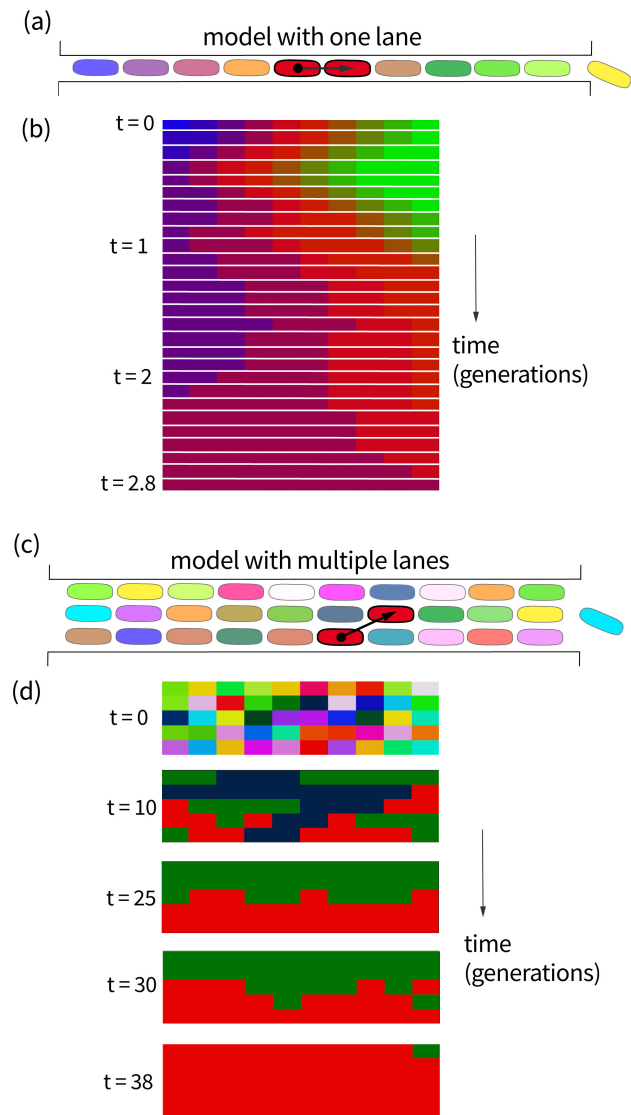


FIG. 2. (a) Model with one lane. A randomly chosen cell reproduces to the right (arrow) and pushes all the cells to the right toward the right end of the microchannel. As a result, the cell next to the right end is expelled from the microchannel. Different colors represent different clonal populations. (b) Dynamics of the model with one lane. Colors represent clonal populations. The population starts at $t = 0$ with N clonal populations, each consisting of 1 cell and continues until one of them takes over the entire population. (c) Model with multiple lanes. Here a newborn cell can take a position in a neighbor lane. (d) Dynamics of the model with multiple lanes. Colors have the same meaning as in (b). After some time, there are two competing clonal populations with segregation along the microchannel similar to Fig. 1a.

where $\gamma \approx 0.577$ is the Euler–Mascheroni constant, and the approximation is valid for large N . We shall prove this result in Section VI. The logarithmic dependence on the system size in Eq. (1) implies that fixation in this

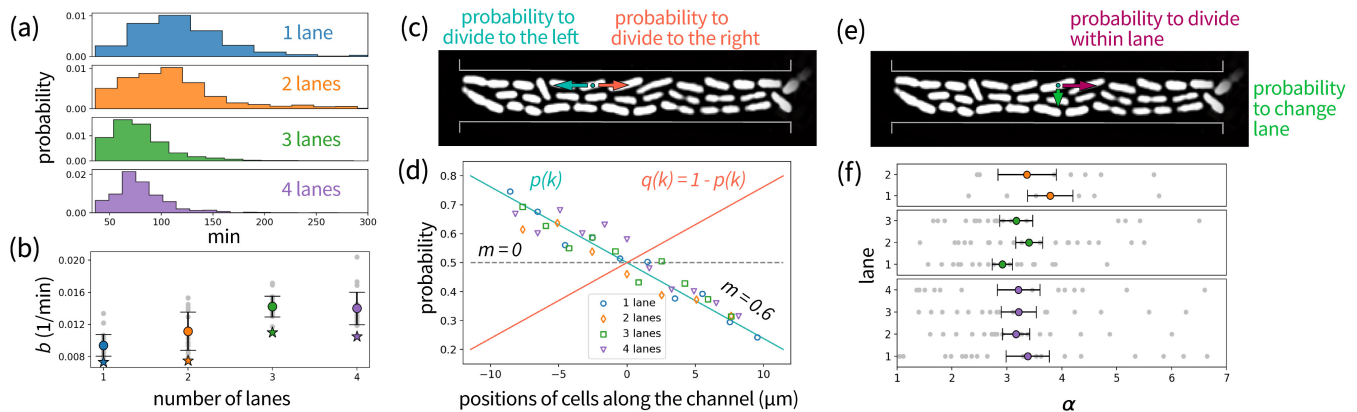


FIG. 3. (a) Empirical distributions of division times $f_E(\tau)$ obtained from the experiments with 1, 2, 3 and 4 lanes. (b) Division rates evaluated from the experimental data. The error bars represent the mean value and the standard deviation of the division rates obtained as the inverse of the mean generation time over the population in a single experimental run. The stars mark the effective population growth rates b evaluated from the Euler-Lotka equation (5). (c) Schematic representation of the two possible directions of division. We interpret an asymmetry between frequencies of reproductions in these two directions as an effect of inertia. (d) Effect of inertia observed in the experimental data. The scattered points represent the frequencies of divisions to the left in the data with 1, 2, 3 and 4 lanes of bacteria. We fit the data with the linear function given in Eq. (2) using the least squares method, resulting in $m = 0.6$. Dashed line represent the case with no inertia effect ($m = 0$). (e) Schematic representation of division within the same lane and to a neighbor lane. (f) Horizontal preference of cells divisions observed in the experimental data. The error bars represent the mean value and the standard error of the parameter α evaluated from each lane in the experimental data. The average value over all experiments is $\alpha = 3.2$.

system is an extremely fast process. For comparison, in populations described by voter (or stepping-stone) models, the average fixation time scales as N^2 . We will examine in details causes and consequences of this fact.

We now consider the case with multiple lanes, see Fig. 2c. In the model with multiple lanes, daughter cells can also land in lanes adjacent to that of their mothers. Cells located at one of the solid boundaries of the microchannel have 5 possible destination sites for their daughter cells. Daughters of cells located strictly inside the microchannel can end up in 8 possible lattice sites. Each of the available sites is chosen at random and determine the direction of shift within the same or one neighboring lane. The dynamics of the model with multiple lanes is illustrated in Fig. 2d.

IV. GENERAL MODEL

The assumption of uniform reproduction in Section III needs to be relaxed to quantitatively describe our experiments. In this section, we introduce a general model, where the probabilities of reproducing in different directions are in general non uniform. As for the model with uniform reproduction, we assume that all cells reproduce at a constant rate b .

In general, reproductions to the right or to the left require pushing a different number of cells. We assume that, as effect of inertia, reproductions events that require pushing fewer cells are more likely to occur. We

accordingly introduce a parameter $m \geq 0$ quantifying this effect. Increasing m biases reproduction in the direction closer to an open end.

In the general model with one lane, a cell at position $1 \leq i \leq N$ reproduces to the left and right with probabilities $p(i)$ and $q(i)$, respectively. These probabilities depend on the inertia parameter m and are given by

$$p(i) = \frac{im}{N-1} + \frac{m(N+1)+N-1}{2(N-1)}, \quad q(i) = 1-p(i). \quad (2)$$

In the limiting case $m = 0$, inertia does not affect cell division and $p(i) = q(i) = 1/2$ as in the uniform reproduction model. Imposing that the probabilities in Eq. (2) remain nonnegative leads to the condition $m \leq 1$.

We now introduce the general model with multiple lanes. We assign to each cell its coordinates i, j , with $1 \leq i \leq N$ and $1 \leq j \leq M$. In the following, we refer to the coordinate i as the “horizontal” or “axial” coordinate. We define the reproduction probability $k_{(i',j')(i,j)}$ that the daughter of a cell at position i, j is placed at position i', j' .

In the case of multiple lanes, the parameter m quantifies the effect of inertia as for the one lane case. We introduce an additional parameter $\alpha > 0$ quantifying the preference of cells to reproduce within their lane rather than into another lane as effect of alignment and of the geometry of the microchannel.

We first discuss reproduction probabilities for mother cells in the bulk of the population, i.e., with coordinates satisfying $1 < j < M$. In this case, the daughter can end

up in 8 different positions. We express the reproduction probabilities as

$$\begin{aligned}
k_{(i-1,j)(i,j)} &= \alpha \frac{-2mi + m(N+1) + N - 1}{2(N-1)(\alpha+3)}, \\
k_{(i+1,j)(i,j)} &= \frac{2\alpha}{2(\alpha+3)} - k_{(i-1,j)(i,j)}, \\
k_{(i-1,j-1)(i,j)} &= k_{(i-1,j+1)(i,j)} = \frac{k_{(i-1,j)(i,j)}}{\alpha}, \\
k_{(i+1,j-1)(i,j)} &= k_{(i+1,j+1)(i,j)} = \frac{k_{(i+1,j)(i,j)}}{\alpha}, \\
k_{(i,j-1)(i,j)} &= k_{(i,j+1)(i,j)} = \frac{1}{2(\alpha+3)}.
\end{aligned} \tag{3}$$

If the daughter is placed at the same i coordinate as the mother, the corresponding lane of cells is pushed to the left or right with probabilities given by Eq. (2).

The reproduction probabilities for a mother next to the top boundary of the microchannel ($j = 1$) are expressed by

$$\begin{aligned}
k_{(i-1,1)(i,1)} &= \alpha \frac{-2mi + m(N+1) + N - 1}{(N-1)(2\alpha+3)}, \\
k_{(i+1,1)(i,1)} &= \frac{2\alpha}{2\alpha+3} - k_{(i-1,1)(i,1)}, \\
k_{(i-1,2)(i,1)} &= \frac{k_{(i-1,1)(i,1)}}{\alpha}, \\
k_{(i+1,2)(i,1)} &= \frac{k_{(i+1,1)(i,1)}}{\alpha}, \\
k_{(i,2)(i,1)} &= \frac{1}{2\alpha+3}.
\end{aligned} \tag{4}$$

The reproduction probabilities for a mother next to the bottom boundary ($j = M$) can be similarly expressed. In all cases, if the i coordinate of the daughter ends up being equal to 0 or $N + 1$, she is immediately expelled from the microchannel. In the limiting case $\alpha = 1$ and $m = 0$, the probabilities in Eqs. (3) and (4) are uniform as in the model discussed in Section III.

Summarizing, the general model is determined by the following parameters: M (number of lanes), N (numbers of cells per lane), b (effective division rate), m (inertia parameter), and α (alignment parameter). In the next subsections, we discuss these parameters in more details and fit their values from the experiments.

A. Number of lanes and number of cells per lane

Our microchannels have the same length but different widths, thereby harboring different number of lanes of bacteria, see Section II. This number of lanes ranges from 1 to 4, see supplementary video. The number of cells within each lane fluctuates among different microchannels. We evaluate the average number of cells per lane as the total number of cells found by the detection algorithm in each frame divided by the number of lanes. For

microchannels harboring 1, 2, 3 and 4 lanes, we find that the number of cells per lane are 13 ± 1 , 8.8 ± 0.5 , 9 ± 1 and 9.2 ± 0.5 , respectively. The significantly higher number of cells in the microchannels with one lane is possibly due a lower diffusion of nutrients, causing cells to achieve a smaller average size. Accordingly, for our general model, we consider the four cases $(M, N) = (1, 13)$, $(2, 9)$, $(3, 9)$ and $(4, 9)$.

B. Effective division rate

In our model, cells reproduce in age-independent manner with a constant division rate b . We call $f_E(\tau)$ and $f_M(\tau)$ the distributions of times between consecutive cell division in the experiments and in the model, respectively. The assumption of a constant division rate implies $f_M(\tau) = be^{-b\tau}$. However, the distributions $f_E(\tau)$ are markedly non-exponential, see Fig. 3a. In this section, we associate an effective division rate with such non-exponential distributions and estimate it from the experiments.

In the model, the average number of cells, including those that are expelled, grows exponentially as $n(t) = n(0)e^{bt}$. Since we are working in nutrient-rich conditions, the total number of cells in our experiments grows exponentially as well. We impose that the exponential growth rate in the model must be equal to that in the experiments. For a given distribution $f_E(\tau)$, this condition leads to the Euler-Lotka equation [26]

$$2 \int_0^\infty f_E(\tau) e^{-b\tau} d\tau = 1. \tag{5}$$

This condition defines the effective division rate b . We estimate the distributions $f_E(\tau)$ for each microchannel width from our experiments, see Fig. 3a. We then estimate b by numerically solving Eq. (5) in each case. We find that the effective division rate increases as a function of the microchannel width, see Fig. 3b. This effect might be due to lower diffusion of nutrients inside thinner microchannels and is consistent with the observation that the microchannels with one lane tend to accommodate more cells per unit length, see Section IV A. The effective division rates evaluated with the Euler-Lotka equation are significantly smaller than the averages of the inverse mean generation times for each population obtained experimentally. The reason is that, statistically, fast-reproducing cells provide a larger contribution to the population growth rate [16].

C. Inertia parameter

Our experiments reveal a bias in the frequency of divisions to the left or right depending on the horizontal coordinate of the dividing cell, see Fig. 3c. In particular, we find that cells preferentially reproduce towards the

closest open end. Also in this case, we analyze experimental data with different number of lanes separately. However, we find that the effect of inertia weakly depends on the microchannel width, see Fig. 3d. Our experimental results suggest that the directional bias in the division probability linearly depends on the total mass of cells that the newborn cell would push, consistent with Eq. (2), see Fig. 3d. We evaluate the slope of the functions given in Eq. (2) from the experimental data and find the best fit value $m = 0.6$, see Fig. 3d.

D. Alignment parameter

In our experiments, cells tend to align horizontally. Because of the stability of this alignment, cells preferentially divide within the same lane rather than changing lane, see Fig. 3e. We quantify this effect by the ratio α between the probability of a cell division within a lane to that of a cell division involving a change of lane. If $\alpha = 1$, these probabilities are the same as in the model with uniform reproduction. In the opposite limiting case $\alpha = \infty$, cells are bound to proliferate within their original lane. In this scenario, each lane evolves independently and fixation of the entire population never occurs.

We find that the value of α estimated from the experiments does not differ significantly among microchannels of different width and between cells close to the channel boundaries or in the bulk, see Fig. 3f. Consequently, for our model we set $\alpha = 3.2$, i.e., equal to the average value in our experiments for all channel widths.

V. LOSS OF GENETIC DIVERSITY

A. Dynamics of interfaces

We now study competition among clonal populations in the model with one lane of N cells. This problem can be elegantly treated by focusing on the interfaces between clonal populations. We assign to each cell at position i at time t the position $f_i(t)$ of its ancestor at time $t = 0$. Two neighboring cells having the same value of $f_i(t)$ are therefore conspecific, i.e. they belong to the same clonal population. We assign interfaces to neighboring cells that are not conspecific. We encode these interfaces into a vector $\vec{\sigma}(t) = (\sigma_1(t), \sigma_2(t), \dots, \sigma_{N-1}(t))$, whose components are defined by

$$\sigma_i(t) = \begin{cases} 0 & \text{if } f_i(t) = f_{i+1}(t), \\ 1 & \text{if } f_i(t) \neq f_{i+1}(t). \end{cases} \quad (6)$$

The initial condition for the vector of interfaces is $\vec{\sigma}(0) = (1, 1, \dots, 1)$. The vector of interfaces evolves until it reaches the absorbing state $(0, 0, \dots, 0)$ that corresponds to fixation of one clonal population. Each cell division creates a pair of conspecific cells and shifts all cells either to their right or left by one position. This event implies

that one interface $\{\sigma_i\}_{i=1, \dots, N-1}$ is set to 0 and all interfaces on one side of this position are shifted by one position toward right or left, depending on the direction of the cell division. As a consequence, an interface located at the open end can be removed from the vector. This process is illustrated in Fig. 4.

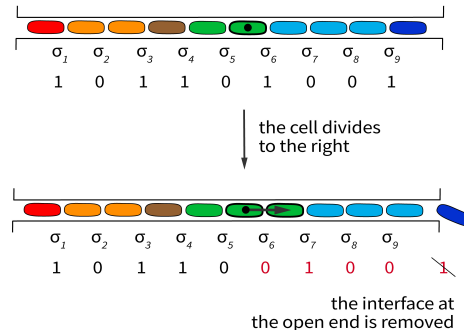


FIG. 4. Dynamics of interfaces as a result of a cell division. The figure shows an example of a cell division; different colors correspond to different clonal populations. Interfaces $\sigma_1, \sigma_2, \dots, \sigma_{N-1}$ are associated with adjacent cells. An interface σ_i is equal to 1 if the two associated cells belong to different clonal populations and zero otherwise. As a consequence of cell division, an interface of value 0 is created at $i = 6$ and a portion of the vector of interface is shifted (in red). As an outcome, one interface is expelled from the system.

To describe the time evolution of the interfaces, we consider the states that can lead to a generic state $\vec{\sigma}(t) = (\sigma_1, \sigma_2, \dots, \sigma_{N-1})$ via one cell division. To this aim, we introduce inverse shift operators that take into account the presence or absence of an interface at the open end:

$$\begin{aligned} \hat{b}_r^i \vec{\sigma} &= (\sigma_1, \sigma_2, \dots, \sigma_{i-1}, \sigma_{i+1}, \dots, \sigma_{N-1}, 0), \\ \hat{b}_l^i \vec{\sigma} &= (0, \sigma_1, \sigma_2, \dots, \sigma_{i-1}, \sigma_{i+1}, \dots, \sigma_{N-1}), \\ \hat{c}_r^i \vec{\sigma} &= (\sigma_1, \sigma_2, \dots, \sigma_{i-1}, \sigma_{i+1}, \dots, \sigma_{N-1}, 1), \\ \hat{c}_l^i \vec{\sigma} &= (1, \sigma_1, \sigma_2, \dots, \sigma_{i-1}, \sigma_{i+1}, \dots, \sigma_{N-1}). \end{aligned} \quad (7)$$

A state $\hat{b}_r^i \vec{\sigma}$ or $\hat{c}_l^i \vec{\sigma}$ evolves to a state $\vec{\sigma}$ if the i -th cell divides to the right. Similarly, a state $\hat{b}_l^i \vec{\sigma}$ or $\hat{c}_r^i \vec{\sigma}$ evolves to a state $\vec{\sigma}$ if the $(i+1)$ th cell divides to the left. We write the master equation for the interface distribution in the general model with one lane, see Eq. (2), in the form:

$$\begin{aligned} \frac{dP_{\vec{\sigma}}}{dt} &= -b \sum_{i=1}^{N-1} [q(i) + p(i+1)] P_{\vec{\sigma}}(t) \\ &+ b \sum_{i=1}^{N-1} \delta_{\sigma_i, 0} [q(i) (P_{\hat{b}_r^i \vec{\sigma}} + P_{\hat{c}_r^i \vec{\sigma}}) + p(i+1) (P_{\hat{b}_l^i \vec{\sigma}} + P_{\hat{c}_l^i \vec{\sigma}})], \end{aligned} \quad (8)$$

where the Kronecker delta takes care of the fact that a reproduction event necessarily creates an interface of

value equal to 0. The solution of Eq. (8) reads

$$P_{\bar{\sigma}} = \prod_{i=1}^{N-1} [\sigma_i e^{-\beta t} + (1 - \sigma_i)(1 - e^{-\beta t})], \quad (9)$$

where we define

$$\beta = b \left(1 - \frac{m}{N-1}\right). \quad (10)$$

The solution given in Eq. (9) can be verified by direct substitution into Eq. (8), see Methods section XI C. Therefore, the interfaces $\{\sigma_i(t)\}_{i=1,\dots,N-1}$ are independent, identically distributed random variables with $P(\sigma_i(t) = 1) = e^{-\beta t}$ for all i . The characteristic rate β at which interfaces are lost reduces to the effective division rate b for $m = 0$. For $m > 0$, this characteristic rate becomes slower than the effective division rate due to the effect of inertia.

B. Number of clonal populations

If the initial population is genetically diverse, the speed at which the number of clonal populations decreases in time can be interpreted as the pace at which this diversity is lost. We study this process starting from the general model with one lane, where we make use of the interface formalism developed in the previous subsection. In this case, the number of clonal population is related to the number of interfaces by

$$A(t) = \sum_{i=1}^{N-1} \sigma_i(t) + 1, \quad (11)$$

with the initial condition $A(0) = N$. Fixation is reached when $A(t) = 1$, which is an absorbing state for the number of clonal populations. Using Eq. (9), we find that the averaged number of clonal populations at time t is equal to

$$\langle A(t) \rangle = (N-1)e^{-\beta t} + 1. \quad (12)$$

Populations with multiple lanes are characterized by a fast horizontal dynamics along the lanes. Competition among lanes is a slower process, whose speed is tuned by the parameter α , see Section IV D. In particular, for sufficiently large α , lanes weakly interact. In this limit, it follows from Eq. (12) that the average number of clonal populations at time t is expressed by

$$\langle A(t) \rangle \approx M(N-1)e^{-\beta t} + M. \quad (13)$$

Equation (13) describes the decay of the number of clonal populations up to the value $\langle A(t) \rangle = M$, and can be cast in the scaling form

$$\ln \frac{\langle A(t) \rangle - M}{M(N-1)} \approx -\beta t. \quad (14)$$

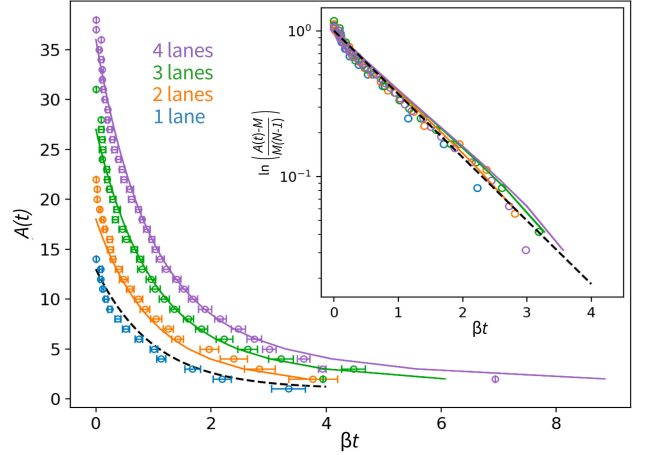


FIG. 5. Number of clonal populations as a function of dimensionless time βt . The scattered points with error bars represent the experimental data. The solid curves correspond to numerical simulations. The dashed curve shows the theoretical result of Eq. (12) for $M = 1$. Time in the experimental data is scaled by the effective division rate evaluated for each group of data with 1, 2, 3 and 4 lanes, see Section IV. Parameters are $m = 0.6$ and $\alpha = 3.2$, see Section IV. The inset shows the rescaled experimental observations and numerical simulations according to Eq. (14).

The predictions of the general model on the number of clonal populations are in excellent agreement with experiments, see Fig. 5. In the case of one lane, we compared the experiments with the analytical solution given in Eq. (12). For multiple lanes, we compared experiments with numerical simulations, since the solution given in Eq. (13) is only approximated. Despite this approximation, we find that the scaling form embodied in Eq. (14) is consistent with the experimental results for all microchannel widths, see inset of Fig. 5.

VI. FIXATION TIME

The fixation time of a population with M lanes and N cells per lane is equal to the time it takes to expel $(MN-1)$ clonal populations from the microchannel. We start from the model for one lane, $M = 1$, and study the time $T_{A \rightarrow A-1}$ it takes to expel the A th clonal population, with $A = N, \dots, 2$. Using Eq. (9) and Eq. (11), we obtain that the times $T_{A \rightarrow A-1}$ are exponentially distributed with mean $\langle T_{A \rightarrow A-1} \rangle = 1/[\beta(A-1)]$. The average fixation time is equal to the sum of the averages of these times:

$$\langle T_{\text{fix}} \rangle = \beta^{-1} \sum_{A=2}^N \frac{1}{A-1} \approx \beta^{-1} [\log(N-1) + \gamma], \quad (15)$$

where $\gamma \approx 0.577$ is the Euler–Mascheroni constant, and approximation is valid for large N . For the uniform re-

production case $m = 0$, Eq. (15) yields the result anticipated in Eq. (1).

It is interesting to compare the result of Eq. (9) with the equivalent result for traditional models in spatial population genetics such as the stepping stone model [18]. In the one-dimensional stepping stone model, interfaces behave as random walkers, so that the dependence $\langle T_{\text{fix}} \rangle \sim N^2$ is a byproduct of diffusive scaling. Here instead, the pushing dynamics cause interfaces to decay exponentially regardless of the system size, greatly speeding up fixation.

We now move to populations with multiple lanes, $M > 1$. It is convenient to analyze them starting from the limiting case $\alpha \rightarrow \infty$. In this limit, each lane reaches its fixation state independently. The fixation time within each lane is still given by Eq. (15). We introduce the time $T_{\text{fix}}^{\text{ind}}$ at which each lane has reached its fixation state. Note that this is different from the ‘‘global’’ fixation time $T_{\text{fix}}^{\text{fix}}$, since at the time $T_{\text{fix}}^{\text{ind}}$ different lanes might still host different clonal populations. We find that the average of $T_{\text{fix}}^{\text{ind}}$ is expressed by

$$\langle T_{\text{fix}}^{\text{ind}} \rangle \approx \beta^{-1} [\log(M(N-1)) + \gamma], \quad (16)$$

see Methods section XID. Since cells never leave their original lanes, fixation of the entire population is never reached.

For large but finite α , there is some degree of competition between lanes. The competition dynamics among lanes can be approximated by a linear invasion process with M sites and transition rates that depend on the parameter α . Using such approach, we calculate the fixation time of the entire populations for $M = 2, 3$ and 4 and find that it grows linearly with α , see Methods section XID.

The fixation time in the experiments with one lane is in good agreement with the theoretical prediction given by Eq. (15). Equation (15) predicts an average fixation time of 3.2 ± 1.2 generations for $m = 0.6$ and $N = 13$, compared with 3.6 ± 1.0 generations for our experiments, see Fig. 5. Numerical simulations of our model predict a longer fixation time at increasing number of lanes (7.86 ± 4.18 , 14.81 ± 8.45 , 23.8 ± 14.1 for 2, 3, and 4 lanes, respectively). We did not observe fixation in our experiments with multiple lanes. This is consistent with the fact that the typical length of our experiments in these cases (5.2 ± 2.8 , 6.2 ± 1.4 and 3.2 ± 0.9 generations for 2, 3, and 4 lanes, respectively) are shorter than the typical predicted fixation times in each case.

VII. MOTHER MACHINE

The interface formalism can be directly applied to a model for the mother machine. This model is very similar to our model with one lane. The main difference is that, in the mother machine, reproductions can occur in only one direction since one end of the microchannel is sealed. Without loss of generality, we assume that the

open end is the right one. Therefore, the vector of interfaces evolves according to a master equation including only right inverse shift operators:

$$\frac{dP_{\vec{\sigma}}}{dt} = -b(N-1)P_{\vec{\sigma}}(t) + b \sum_{i=1}^{N-1} \delta_{\sigma_i,0} (P_{b_i^i \vec{\sigma}} + P_{c_i^i \vec{\sigma}}). \quad (17)$$

The solution to this master equation also factorizes

$$P_{\vec{\sigma}} = \prod_{i=1}^{N-1} [\sigma_i e^{-bt} + (1 - \sigma_i)(1 - e^{-bt})]. \quad (18)$$

Interestingly, the temporal behavior of the number of interfaces is the same for the case with one and two open ends. This result implies that the average fixation time for a population with N cells with two open ends given in Eq. (1) also holds for the mother machine.

VIII. FIXATION PROBABILITIES

We define the fixation probability $P_{i,j}^{\text{fix}}$ as the probability that a clonal population takes over the entire population, as a function of the coordinates i, j of the initial individual. We find that, in the model with one lane and uniform reproduction, the fixation probabilities follows a binomial distribution

$$P_i^{\text{fix}} = \binom{N-1}{i-1} 2^{1-N}. \quad (19)$$

In the general model with one lane, the fixation probabilities follow a hypergeometric distribution, see Methods section XIE. For large N , both these distributions can be approximated with a Gaussian distribution with mean $\mu_N = (N-1)/2$ and variance $\sigma_N^2 = (1-m/2)(N-1)/4$. This implies that, at increasing effect of inertia, mutants that are most likely to take over the population are located in a narrower and narrower region at the center of the microchannel, see Fig. 11b. For example, for a population with $N = 50$ cells and uniform reproduction, only 14 cells in the middle have more than 95% of chances to fixate. In the case of presence of inertia ($m = 0.6$), this number reduces to 12.

In the general model with multiple lanes, the fixation probabilities can be approximated by

$$P_{i,j}^{\text{fix}} \approx \begin{cases} \frac{2\alpha + 6}{M(2\alpha + 3) + 6} \phi_{\mu_N, \sigma_N^2}(i) & \text{if } j = 1, M, \\ \frac{2\alpha + 3}{M(2\alpha + 3) + 6} \phi_{\mu_N, \sigma_N^2}(i) & \text{otherwise,} \end{cases} \quad (20)$$

where $\phi_{\mu_N, \sigma_N^2}(j)$ is a Gaussian distribution with mean $\mu_N = (N-1)/2$ and variance $\sigma_N^2 = (1-m/2)(N-1)/4$, see Fig. 6a. The approximation in Eq. (20) is valid in the limit of large N and α .

The latter limit allows describing the competitive dynamics among lanes as an invasion process, see Methods

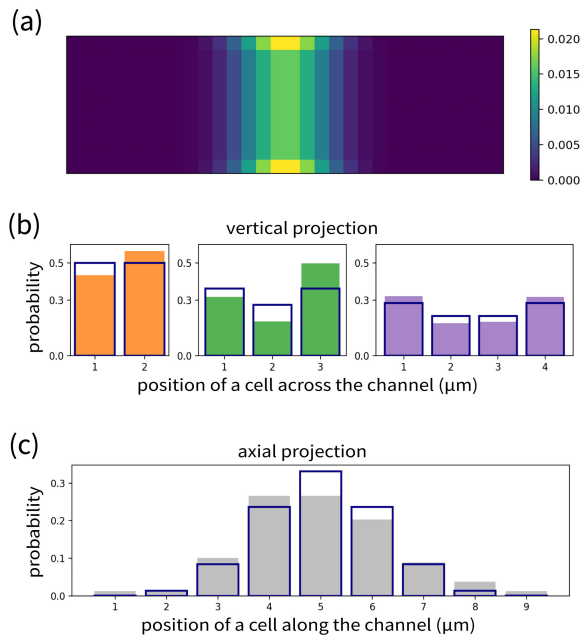


FIG. 6. (a) Fixation probabilities predicted by Eq. (20) for $M = 10$, $N = 30$. (b) Projections of the fixation probabilities along the vertical (across the channel) axis. Color bars represent the experimental observations, the dark blue bars represent the sums over j of the analytical solution of Eq. (20). (c) Projections of the fixation probabilities along the axial direction of microchannel. Grey histogram represents the experimental observations, dark blue bars represent the sums over i of the analytical solution given in Eq. (20).

section XID. The effective advantage of cells next to the boundaries expressed by Eq. (20) descends from properties of the invasion process in a finite system. This boundary effect becomes less pronounced at increasing α .

In the experiments with multiple lanes, we rarely observe fixation. At the last time point of each recording, we typically find 2 to 6 surviving clonal populations. To overcome this shortcoming, we randomly choose a clonal population among the surviving ones, assume it will reach fixation, and therefore use it to evaluate the empirical fixation probabilities. Due to statistical limitations, we project the fixation probability distributions along the vertical direction and along the horizontal direction. In the vertical projections, we separately show datasets with 2, 3 and 4 lanes, see Fig. 6b. In the horizontal projection, we aggregate the data for 1, 2, 3 and 4 lanes since the microchannel length is the same in all these cases, see Fig. 6c. The empirical distributions agree very well with the theoretical prediction of Eq. (20).

IX. SELECTIVE ADVANTAGE

If a mutation carrying a selective advantage arises in a finite, well-mixed population, the fate of the mutants depends on the balance between the strength of the selective advantage and random drift. The spatial structure of a population may affect this balance. In this section, we theoretically study the strength of selection in microchannels with one lane of cells.

Since we neglect death events, mutant populations can only be lost by being expelled at the open ends of the microchannel. Eventually, a mutant population will reach one of the open ends and compete for fixation with the non-mutant cells. Therefore, we focus on the simple scenario in which the two populations occupy a portion of the microchannel adjacent to each open end, see Fig. 7a. Without loss of generality, we assume that the population on the right is the wild type population, with reproduction rate b as before. The population on the left is constituted by mutants with reproduction rate $b(1+s)$, where s is the selection coefficient. We call x_0 the initial number of mutants and $p = x_0/N$ the initial frequency of mutants. For large N , we find that the probability that the mutants take over the channel is expressed by

$$\pi_N(p) = \frac{\gamma(z, w(ps+1)) - \gamma(z, w)}{\gamma(z, w(s+1)) - \gamma(z, w)}, \quad (21)$$

where $\gamma(x, y) = \int_0^y t^{x-1} e^{-t} dt$ is the lower incomplete gamma function, $w = 2N(2+s)/s^2$, and $z = 1+4N(1+s)/s^2$, see Methods section XIF.

The expression of the fixation probability given in Eq. (21) is a steep function of the initial fraction $p = x_0/N$ of mutants, see Fig. 7b. If this fraction is much smaller than 0.5, mutants are very likely to be expelled, whereas if it is much larger than 0.5 they are very likely to take over. This conclusion is rather insensitive to the value of s , at least for selection coefficients in the range of typical beneficial mutations in *E. coli* [27]. This fact is related with the high positional advantage of cells at the center of the microchannel, see Section VI. For $p = 0.5$, the mutant fixation probability increases as a function of the selection coefficient s and the population size N , see Fig. 7c. Equation (21) predicts that the fixation probability depends on the compound parameter Ns^2 , as shown in Fig. 7d.

The dependence on the parameter Ns^2 is in contrast with the dependence on Ns in the case of well-mixed populations, as derived by Kimura [28]. In the well-mixed case, if $Ns \gg 1$, the selective advantage significantly biases the fixation process. In the opposite regime $Ns \ll 1$, fluctuations due to finiteness of the population dominate. This result means that mutations conferring selective advantages smaller than $1/N$ are not likely to be fixated and contribute to the evolution of the population. In microchannels, the same line of thought leads to conclude that selective advantages need to be larger than $1/\sqrt{N}$ in order to reach fixation. In practice, our result implies

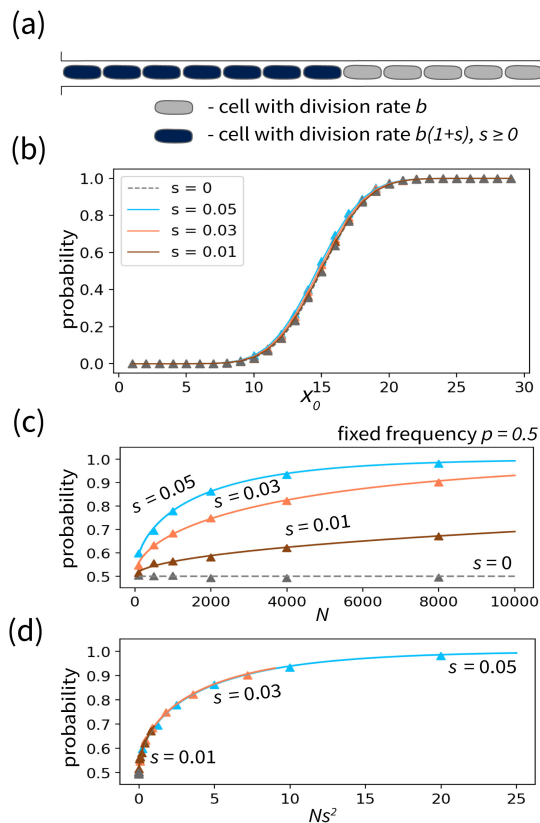


FIG. 7. (a) Two competing populations with reproduction rates b and $b(1+s)$ in a microchannel. (b) Fixation probabilities given in Eq. (21) as a function of x_0 for $N=30$ and different values of the selection coefficient s as a function of the number of selectively advantageous cells at $t=0$. Solid lines represent the theoretical solution, triangle-shape points represent numerical simulations. (c) Fixation probabilities as a function of the number of cells N for fixed initial frequency $p=0.5$ of the mutants and different values of s . (d) Fixation probabilities rescaled as a function of Ns^2 .

that evolution in a microchannel is much less effective than in a well-mixed system.

X. DISCUSSION

In this study, we developed a theory of population genetics for microbes proliferating in microchannels. We base our theory on microfluidic experiments with *E. coli* populations growing in straight microchannels with two open ends. Our experiments reveal that population dynamics generates stripes of clonal populations inside the microchannels. This result is in sharp contrast to the case of bacterial populations growing on agar plates, where competing populations organize into sectors whose boundaries perform random walks [29]. Our theory shows that the peculiar pattern we observe in our experiment is an outcome of pushing dynamics. This dynamics, combined with the geometry of the microchannels, causes a

fast exponential loss of genetic diversity, rapid fixation within each lane, and slower competition among lanes. Because of the ordered population structure inside the microchannels, our lattice model quantitatively predicts the dynamics of diversity loss with remarkable accuracy.

A basic ingredient of our model is the fact that reproducing cells push entire lanes of other cells. Previously, Allen and Novak studied a similar dynamics on a one dimensional ring [24], concluding that this structure does not significantly affect selection strength. In contrast, in a model of epithelial tissues, it was concluded that the pushing dynamics suppresses selection [23]. The reason is that, in this latter model, cells are arranged in a linear array and can be expelled only on one end. Therefore, the cell next to the opposite end possesses a large positional advantage, in a similar fashion as in the mother machine [15]. Random mutations of this cell are very likely to reach fixation, regardless of whether they confer a selective advantage, they are deleterious, or neutral. Conversely, fixation probabilities of mutations occurring elsewhere are very small.

Our results show that, indeed, selection is generally suppressed when microbial populations grow in confined geometries. In particular, this fact holds in channels with two open ends and harboring multiple lanes of cells. We have shown that, in these systems, cells located in a narrow region in the middle of the microchannel possess a large positional advantage over others. The outcome of such uneven positional advantage can be interpreted as an effective random drift slowing down the evolution of the population.

Our model can be extended to other scenarios, for example to competition between non-neutral clonal populations characterized by finite death rates. This generalization is relevant for the dynamics of cancer progression in tissues [10], as cells that carry tumor-promoting mutations often reproduce faster. In these tissues, cells can be eliminated by apoptosis or they can be killed by surrounding cells. In this case, competition of clonal populations depends on their relative fitnesses once they are in contact with each other [30, 31]. A study of such dynamics can provide new insights into how population structure shapes evolution [32, 33]. Another interesting question is whether our results are applicable for populations growing in wide channels. In such populations the ordered lane structure is disrupted at large scales, potentially leading to jamming [34, 35]. Modeling this effect would require generalizing our lattice model to continuous space.

The fact that a constrained geometry has such a drastic impact on population genetics should be taken into account when designing experimental evolutionary studies that use microfluidic devices. Our results open interesting venues in constraining evolution by shaping the geometry of a microchannel hosting an evolving population.

ACKNOWLEDGMENTS

We gratefully acknowledge support of the Okinawa Institute of Science and Technology Graduate University (OIST) with subsidy funding from the Cabinet Office, Government of Japan. We thank colleagues from the Micro/Bio/Nanofluidics Unit at OIST: Daniel Carlson for assistance in numerical simulation and Riccardo Funari for fruitful discussion. We thank Maria Emily and Kang-Yu Chu for assistance in microfabrication. We thank Professor Paola Laurino from OIST for gifting the MG1655 bacterial strain. We thank Deepak Bhat and Robert Ross for feedback on a preliminary version of the paper. A.Q.S. acknowledges funding from the Japan Society for the Promotion of Science (JSPS, Grant Nos. 18H01135).

XI. METHODS

A. Experimental setup

Bacteria strains and maintenance. MG1655, a derivative of *E. coli* K-12 wild-type strain, was used in this study. We transformed in MG1655 a plasmid to constitutively express green fluorescence protein (GFP) (pUA66 PrpsL-GFP KanR) to allow tracking single bacteria. Dr. Pamela Silver from Harvard University kindly gifted pUA66 PrpsL-GFP [36]. For visualization with the red fluorescence marker for the same strain of MG1655, pUA66 plasmid with mCherry open reading frame replacing that of GFP was constructed by VectorBuilder. We cultured the MG1655 hosting pUA66 plasmids in Luria-Bertani (LB) broth (Lennox) supplemented with 50 $\mu\text{g mL}^{-1}$ Kanamycin. For long term cryopreservation, we stored log phase bacteria suspension supplemented with glycerol to a final concentration of 20% in -80°C . Detailed description of bacteria strains and plasmid engineering is provided in the Appendix .

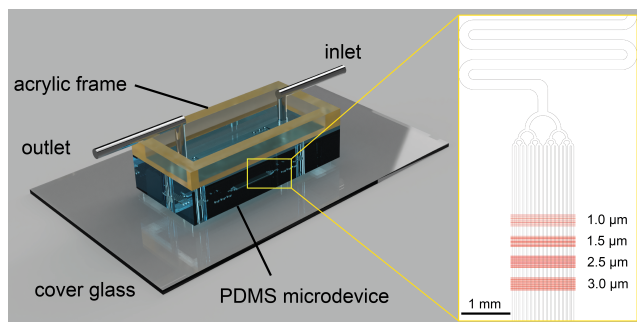


FIG. 8. Composition of the integrated microdevice used to track bacteria lineage in real time. The inset shows half of the symmetric design of microstructures in the PDMS device. The red pattern indicates the growth channels and the black pattern indicates the flow channels that are joined by a tree-like flow stabilizing structure and a flow resistor to an inlet or outlet.

Microfluidic chip design and microfabrication. The poly(dimethylsiloxane) (PDMS) device (on top of the cover glass) consisted of the top flow channels (black patterns, Fig. 8 inset) for nutrients delivery and bacteria removal, and the bottom growth channels (red patterns, Fig. 8 inset) for bacteria growth, removal, and monitoring. In order to perfuse fresh nutrients and create flow to remove bacteria, twenty growth channels of each width were intersected with 16 flow channels ($L \times W \times H = 4500 \times 50 \times 15 \mu\text{m}$). Growth channels ($L \times H = 3 \times 1 \mu\text{m}$) with varying width (1, 1.5, 2.5, and 3 μm) and interspacing of 10 μm were designed for high throughput monitoring on the evolution of bacteria lineage studies such that old bacteria generations could be expelled from both ends in contrast to from a single end design in the mother machine [15, 37]. The flow channels were joined by flow equalizing tree-like channels and flow resistors on both ends [38] and connected to an inlet and an outlet.

A silicone mold with the microstructures designed as above was fabricated by multi-step lithography using negative photoresist (mr-DWL-5, Micro Resist Technology, Germany) and maskless direct writing (DL-1000, NanoSystem Solutions, Japan). Poly(dimethylsiloxane) silicone elastomer microfluidic devices (PDMS Sylgard 184, A:B=10:1, Dow Corning, USA) was fabricated by standard soft lithography [39]. The PDMS slab was first cut and punched with an inlet and outlet using a puncher (Accu-punch, Syneo, USA), then bonded to a high-precision No.1.5H cover glass (Paul Marienfeld, Germany) using plasma activation (Harrick Plasma, USA). A 2 mm-thick acrylic frame was cut with CO₂ laser cutter (Universal Laser Systems, USA) and affixed on top of the PDMS as a reservoir for bacteria seeding, completing the fabrication of the integrated microdevice. The detailed information of design and microfabrication is provided in Appendix .

Bacterial lineage tracking and time-lapse microscopy. Log-phase MG1655 *E. coli* harboring plasmids for fluorescent proteins were grown at 37°C with 200 rpm vigorous shaking in LB broth supplemented with kanamycin until the optical density at 600 nm (OD_{600}) reached 0.2. The bacteria suspension was concentrated 20 times by centrifugation at $3000 \times g$ for 10 minutes. The bacteria suspension was injected into the PDMS microdevice which has been passivated with 2 mg mL^{-1} bovine serum albumin and 0.5 mg mL^{-1} salmon sperm DNA to reduce bacterial binding to the microchannel walls. The bacteria were allowed to enter the growth channels under static condition for 2 hours before the M9 media was infused via tubing using a syringe pump (neMESYS, Cetoni GmbH, Germany). The M9 media contains M9 salts and supplementation of filter-sterilized MgSO_4 , CaCl_2 , glucose, kanamycin, rifapentine, and MEM vitamins, which are low in carbon source to avoid biofilm formation [16, 39, 40]. The M9 media were infused at a flow rate of 1.6 $\mu\text{L min}^{-1}$ and doubled every two hours until it reached 16 $\mu\text{L min}^{-1}$.

The PDMS microdevice was mounted in a microscope on-stage incubator (WKSM, Tokai Hit, Japan) on an inverted motorized epi-fluorescence microscope (Ti-E, Nikon, Japan) with either a 100X oil immersion objective or a 60X oil immersion objective with 1.5X intermediate magnification. The fluorescence images of the bacteria were taken at an interval of $\Delta t = 3$ minutes using a high sensitivity camera (Prime95B, Photometrics, Canada) with GFP or mCherry filter cubes (Semrock, USA). More detailed information is provided in the Appendix .

B. Data processing

Preprocessing. We analyzed the time-lapse recordings of our experiments. The spatial resolution of each image was 0.11 micron/pixel with field of view of 1200×1200 pixels. We filtered microchannels containing smoothly moving and proliferating bacteria during the entire recording using ImageJ software and its plugins [41]. We prepared the data for the processing in three steps. First, we rotated all images in such a way that the boundaries of microchannels are horizontally aligned. This step allows us to compare bacteria orientations among different recordings. Second, we corrected the recording drift using the plugin StackReg [42]. Third, we applied the filter “Unsharp Mask” to reduce noise and increase image contrast.

Finding bacteria contours. From the preprocessed recordings, we determined contours of each bacteria in each frame. We used MicrobeJ plugin that provides an automatic algorithm for detecting bacteria contours and centers using specified information about their morphology [43].

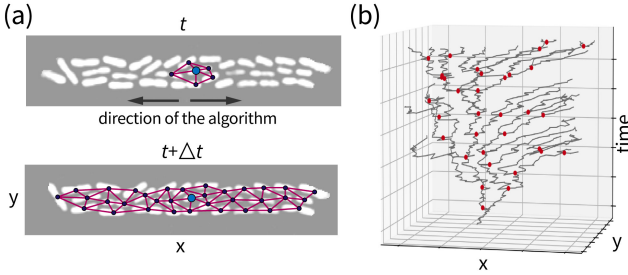


FIG. 9. (a) Local structures of cells constructed on two consecutive images from time-lapse experimental recordings of proliferating *E. coli* in a microchannel. The local structure of a cell from the top image is compared to the local structures of cells from the bottom image. (b) An example of a spatial generation tree of a clonal population constructed from the experimental data after the tracking step. Grey trajectory represents positions of clonal cells in time, red points represent division events.

Tracking. The tracking algorithm identified the same bacteria between consequent frames. Since we worked

with densely packed bacteria in a confined area, we used a tracking algorithm based on construction of local structures and their further comparison [44]. We constructed the local structures as Delaunay meshes with nodes at the centers of the bacteria (Fig. 9a). Delaunay mesh maximizes the minimum angle of the triangles that generate the mesh and it is independent on topology of bacteria. In the algorithm, we compared cells using their positions with respect to other cells in the population rather than the morphological characteristics. Such approach is convenient for dense populations, because cells are in close mechanical interaction between each other. We associated a cell on a frame at time t with the one on the next frame at time $t + \Delta t$ frame by minimizing the difference between their local structures. This is the forward step of the algorithm. The algorithm also includes a backward step to determine division events. In the backward step, all bacteria from a frame at time $t + \Delta t$ that were not associated with any bacteria on t frame were compared to them in the same way in order to determine their mothers. We adapted the algorithm proposed in [44] to reach higher accuracy for our experimental data. Mainly, we modified the similarity measures between local structures and set the specific order of cells comparisons. For growing populations in microchannels with open ends, it was more beneficial to compare cells starting from the center of the microchannel toward open ends, because otherwise we risked making wrong associations at the beginning with the removed cell that could affect further performance of the algorithm, see Fig. 9a. The tracking algorithm returned spatial lineage trees for each cell in the channel. An example of such tree is shown in Fig. 9b. The spatial trees contain all the information about the population dynamics.

C. Distribution of interfaces in the model with one lane

To verify the solution shown in Eq. (9), we substitute it into Eq. (8). We first notice that

$$\begin{aligned} P_{\hat{b}_i \bar{\sigma}}(t) &= P_{b_i \bar{\sigma}}(t) \\ &= \frac{P_{\bar{\sigma}(t)}(1 - e^{-\beta t})}{[\sigma_i e^{-\beta t} + (1 - \sigma_i)(1 - e^{-\beta t})]}, \end{aligned} \quad (22)$$

$$\begin{aligned} P_{\hat{c}_i \bar{\sigma}}(t) &= P_{c_i \bar{\sigma}}(t) \\ &= \frac{P_{\bar{\sigma}(t)} e^{-\beta t}}{[\sigma_i e^{-\beta t} + (1 - \sigma_i)(1 - e^{-\beta t})]}. \end{aligned} \quad (23)$$

Substituting the solution (9) and substituting it into Eq. (8) along with Eqs. (22), (23) and the probabilities given in Eq. (2), we obtain

$$\sum_{i=1}^{N-1} \frac{1 - \sigma_i - \delta_{\sigma_i, 0}}{[\sigma_i e^{-\beta t} + (1 - \sigma_i)(1 - e^{-\beta t})]} = 0. \quad (24)$$

The nominator in this expression is equal to 0 for both $\sigma_i = 0, 1$. Therefore, the solution given in Eq. (9) satisfies Eq. (8).

D. Fixation time in the model with multiple lanes

We consider the model with multiple lanes. If the parameter α is large enough, lanes evolve independently, each of them eventually reaching its fixation state. To estimate the fixation time, we first calculate the average time at which all M lanes have reached their fixation states. We call T_{fix}^j the time at which lane j has reached fixation. We also define $T_{\text{fix}}^{\text{ind}} = \max(T_{\text{fix}}^1, T_{\text{fix}}^2, \dots, T_{\text{fix}}^M)$ the time at which all lanes have independently reached fixation.

Our first step is to compute the distribution of T^{fix} for the model with one lane. The fixation time can be expressed by $T_{\text{fix}} = \sum_{A=2}^N T_{A \rightarrow A-1}$, where the time it takes to expel the A th clonal population $T_{A \rightarrow A-1}$ is exponentially distributed with mean $\langle T_{A \rightarrow A-1} \rangle = 1/[\beta(A-1)]$ and β is defined in Eq. (10). Therefore, T_{fix} is hyperexponentially distributed:

$$\begin{aligned} f(T_{\text{fix}}) &= \sum_{n=1}^{N-1} \prod_{j=1; j \neq n}^{N-1} \frac{j}{j-n} n e^{-\beta n T_{\text{fix}}} \\ &= \sum_{n=1}^{N-1} (-1)^{n-1} \binom{N}{n} n e^{-\beta n T_{\text{fix}}} \\ &= (N-1)(1 - e^{-\beta T_{\text{fix}}})^{N-2} e^{-\beta T_{\text{fix}}}, \end{aligned} \quad (25)$$

and its cumulative distribution function is

$$F(T_{\text{fix}}) = \int_0^{T_{\text{fix}}} f(x) dx = (1 - e^{-\beta T_{\text{fix}}})^{N-1}. \quad (26)$$

In the model with multiple lanes and $\alpha \gg 1$, Eq. (26) governs the distribution of the fixation time T_{fix}^j of each lane independently. Therefore, the distribution of the time $T_{\text{fix}}^{\text{ind}}$ at which all lanes have reach fixation is expressed by

$$\begin{aligned} g(T_{\text{fix}}^{\text{ind}}) &= M f(T_{\text{fix}}^{\text{ind}}) F^{M-1}(T_{\text{fix}}^{\text{ind}}) \\ &= M(N-1) e^{-\beta T_{\text{fix}}^{\text{ind}}} (1 - e^{-\beta T_{\text{fix}}^{\text{ind}}})^{M(N-1)-1}. \end{aligned} \quad (27)$$

The average of $T_{\text{fix}}^{\text{ind}}$ is expressed by

$$\begin{aligned} \langle T_{\text{fix}}^{\text{ind}} \rangle &= \int_0^{\infty} z g(z) dz \\ &= M(N-1) \int_0^{\infty} z e^{-\beta z} (1 - e^{-\beta z})^{M(N-1)-1} dz \\ &= \beta^{-1} \sum_{k=1}^{M(N-1)} \frac{1}{k} \approx \beta^{-1} [\log(M(N-1)) + \gamma], \end{aligned} \quad (28)$$

where γ is the Euler-Mascheroni constant. Once fixation within each lane is reached, the entire system is made up of M competing lanes, each consisting of a single clonal population. The competition dynamics among these lanes can be described by a linear invasion process, see Fig. 10a. We call p_j the rate at which a clonal population in a lane j successfully invades a neighboring lane. We calculate this rate as the sum over all cells in the lane of products of probabilities for a cell to change lane given by Eqs. (3), (4) and fixation probabilities in the new lane given by Eq. (19). For simplicity, we limit ourselves to the case $m = 0$ and obtain

$$p_j \approx \begin{cases} \frac{3b}{2\alpha + 3} & \text{if } j = 1, M, \\ \frac{3b}{2(\alpha + 3)} & \text{otherwise.} \end{cases} \quad (29)$$

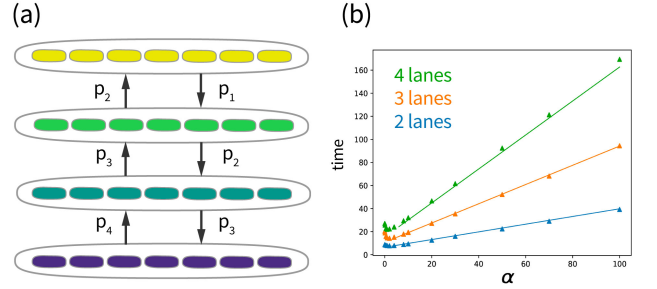


FIG. 10. (a) Scheme of the model with multiple lanes for large α after reaching fixation states within each lane. Nodes represent lanes and arrows represent successful invasion rates, given by Eq. (29). (b) Fixation time as a function of the parameter α . Solid lines represent the theoretical solutions given in Eqs. (30), (31), (32) for $b = 1$, the triangle-shape points represent numerical simulations.

In deriving Eq. (29), we have used that the probabilities P_j^{fix} given in Eq. (19) are normalized and therefore their contribution disappears when summing over all cells in a lane. Note that the characteristic time $1/p_j$ should be interpreted as the typical interval between successful invasion events, but does not include the time required for the invading population to fixate in the new lane.

We now estimate the global fixation time for $M = 2, 3, 4$ lanes as a sum of three contributions. The first is the time at which each lane reaches its fixation state, given by Eq. (28). The second contribution comes from competition between the lanes that we calculate using Eq. (29). The third contribution is the fixation time within each lane that has been successfully invaded. This last contribution is given by Eq. (15). In the case of two lanes, the fixation time is expressed as a sum of these

three contributions by

$$\begin{aligned} \langle T_{\text{fix}}^{N \times 2} \rangle &\approx \frac{1}{b} \left[\log(2(N-1)) + \gamma \right. \\ &\quad \left. + \frac{2\alpha+3}{6} \right. \\ &\quad \left. + \log(N-1) + \gamma \right]. \end{aligned} \quad (30)$$

For simplicity, we report the equivalent expressions for $M = 3$ and $M = 4$ without separating the three contributions. We obtain

$$\begin{aligned} \langle T_{\text{fix}}^{N \times 3} \rangle &\approx \frac{1}{b} \left[\frac{(\alpha+3)(10\alpha+21)}{3(2(\alpha+3)+2\alpha+3)} + 2\log(N-1) \right. \\ &\quad \left. + \log(3(N-1)) + 3\gamma \right] \end{aligned} \quad (31)$$

and

$$\begin{aligned} \langle T_{\text{fix}}^{N \times 4} \rangle &\approx \frac{1}{b} \left[\frac{\alpha+3}{2} \left(\frac{2\alpha+3}{9(\alpha+2)} + \frac{4(\alpha+2)(2\alpha+3)}{3(4\alpha+9)(\alpha+2)+(2\alpha+3)^2} \right) \right. \\ &\quad \left. + \frac{8(5\alpha+9)}{9(2\alpha+3)} \right] + 3\log(N-1) + \log(4(N-1)) + 4\gamma. \end{aligned} \quad (32)$$

Numerical simulations of the model with multiple lanes $M = 2, 3, 4$ and $N = 9$ for large α support the theoretical results of Eqs. (30), (31), (32), see Fig. 10b.

E. Fixation probabilities

In this section, we prove that the fixation probability for the cell at the i th position in the one lane model with N sites and inertia coefficient m has the form

$$P_i^{\text{fix}} = \begin{cases} \frac{\binom{N-1}{i-1}}{2^{N-1}} & \text{if } m = 0, \\ \frac{\binom{N-1}{i-1} \binom{2(N-1)/m - N - 1}{(N-1)/m - i - 2}}{\binom{2(N-1)/m - 2}{(N-1)/m - 1}} & \text{if } m \neq 0, \end{cases} \quad (33)$$

with $i = 1, \dots, N$.

A clonal population originating at the i th position reaches its fixation state if and only if $(i-1)$ cells on its left are expelled from the left end and $(N-i)$ cells on its right are expelled from the right end. Therefore, to find the fixation probability, we calculate the probabilities that the two groups of cells at the left and right of the chosen cell are expelled. We introduce a Markov process $n(t)$ which represents the number of cells to the left of the chosen clonal population, see Fig. 11a. This process has two absorbing states: $n(t) = 0$ implies that the chosen clonal population has reached the left end of the microchannel; $n(t) = N$ implies that the chosen clonal population went extinct. Using Eq. (2), we write the master equation for the process $n(t)$ as

$$\begin{aligned} \frac{dP_n(t)}{dt} &= r_{n+1 \rightarrow n} P_{n+1}(t) + r_{n-1 \rightarrow n} P_{n-1}(t) \\ &\quad - (r_{n \rightarrow n+1} + r_{n \rightarrow n-1}) P_n(t), \end{aligned} \quad (34)$$

where the transition rates are defined by

$$\begin{aligned} r_{n \rightarrow n+1} &= b \sum_{i=1}^n q(i) = b \frac{n[N-1-m(N-n)]}{2(N-1)}, \\ r_{n \rightarrow n-1} &= b \sum_{i=1}^n p(i) = b \frac{(N-n)[N-1-mn]}{2(N-1)}. \end{aligned} \quad (35)$$

We rewrite Eq. (34) with the initial condition $n(0) = n_0$,

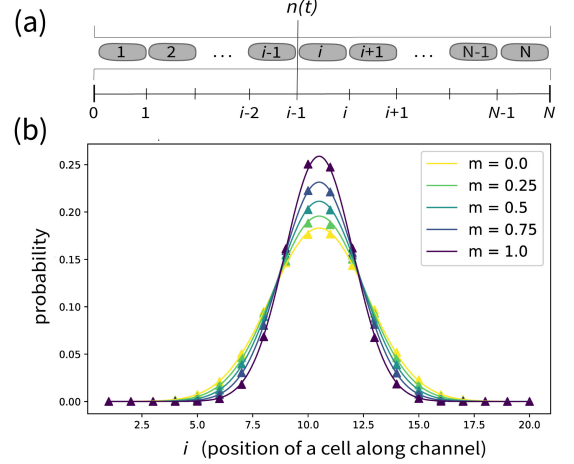


FIG. 11. (a) Scheme of the process $n(t)$. At each time point, $n(t)$ can be at any position $0, \dots, N$. If $n(t)$ reaches the absorbing state 0 (N), the population at the right (left) end fixates. (b) Fixation probabilities for the model with one lane of $N = 20$ cells. Solid curves represent fixation probabilities given in Eq. (33), the triangle-shape points represent numerical simulations of the model with $N = 20$ and different values of m .

$n_0 = 1, \dots, N$ in the matrix form

$$\begin{cases} \partial_t \mathbf{P}(t) = M \mathbf{P}(t), \\ \mathbf{P}(0) = \mathbf{P}_0, \end{cases} \quad (36)$$

where $\mathbf{P}(t) = (P_1(t), P_2(t), \dots, P_N(t))^T$. The initial condition is $P_n(t=0) = \delta_{n,n_0}$. The matrix M is a tridiagonal transition matrix with the following elements on the upper diagonal

$$M_{n,n-1} = b_n = -\frac{b}{2}(N-n-1) \left(1 - \frac{m(n+1)}{N-1} \right), \quad (37)$$

on the main diagonal

$$M_{n,n} = a_n = \frac{b}{2} \left(N - 2mn \frac{N-n}{N-1} \right), \quad (38)$$

and on the lower diagonal

$$M_{n,n+1} = c_n = -\frac{b}{2} n \left(1 - m \frac{N-n}{N-1} \right). \quad (39)$$

The propagator for the process $n(t)$ is expressed by

$$P_{n|n_0}(t) = (e^{Mt})_{n,n_0}. \quad (40)$$

Therefore, the probability flux to the absorbing state N at time t has the form

$$\begin{aligned} J_{N|n_0}(t) &= r_{N-1 \rightarrow N} P_{N-1|n_0}(t) \\ &= \frac{b(N-1-m)}{2} (e^{Mt})_{N-1, n_0}. \end{aligned} \quad (41)$$

The probability of being absorbed in N given the initial state $n_0 = 1, \dots, N$ is equal to

$$P_{N|n_0} = \int_0^\infty J_{N|n_0}(t) dt = -\frac{b(N-1-m)}{2} (M^{-1})_{N-1, n_0}. \quad (42)$$

To write this probability in an explicit form, we use a result for the inverse of a tridiagonal matrix [45]. The $(N-1, k)$ th element of the inverse of the tridiagonal transition matrix M is given by

$$(M^{-1})_{N-1, k} = -\frac{2}{b} \begin{cases} (-1)^{N-1+k} \frac{\phi_N \theta_{k-1}}{\theta_{N-1}} \prod_{i=k}^{N-2} c_i & \text{for } k < N-1, \\ \theta_{N-2} \frac{\phi_N}{\theta_{N-1}} & \text{for } k = N-1, \end{cases} \quad (43)$$

where

$$\theta_k = a_k \theta_{k-1} - b_{k-1} c_{k-1} \theta_{k-2}, \quad i = 2, 3, \dots, N-1, \quad (44)$$

$$\phi_k = a_k \phi_{k+1} - b_k c_k \phi_{k+2}, \quad i = N-2, N-3, \dots, 1, \quad (45)$$

with the boundary values $\theta_0 = 1$, $\theta_1 = a_1$, $\phi_N = 1$, $\phi_{N-1} = a_{N-1}$. Since the upper and lower diagonals are symmetric, $\theta_k = \phi_{N-k}$. Using these expressions, we obtain

$$\begin{aligned} \phi_k &= \frac{(N-1)!}{(k-1)!} \prod_{i=1}^{N-k} u_i \\ &+ (N-k)! \sum_{i=k}^{N-1} \binom{N-1}{i} \prod_{j=0}^{N-i-1} u_j \prod_{j=k}^i u_j, \end{aligned} \quad (46)$$

where $u_i = (1 - m_i)/(N-1)$. Equations (42) and (46) imply that

$$P_{N|n_0} = \frac{\sum_{i=0}^{n_0-1} \binom{N-1}{i} \prod_{j=0}^{N-i-1} u_j \prod_{j=0}^i u_j}{\sum_{i=0}^{N-1} \binom{N-1}{i} \prod_{j=0}^{N-i-1} u_j \prod_{j=0}^i u_j}. \quad (47)$$

An analogous result holds for the group of cells to the right of the chosen clonal population, due to the symmetry of the model. Using these absorbing probabilities, we write the fixation probability as

$$P_i^{\text{fix}} = P_{N|i} - P_{N|i-1}. \quad (48)$$

After some algebra, using Eqs. (47) and (48) we obtain Eq. (33). The theoretical result (33) is confirmed by numerical simulations, see Fig. 11b.

F. Selective advantage

In this section, we prove Eq. (21). We consider two competing connected populations in a microchannel with one lane. One population is constituted by mutants, that reproduce at rate $b(1+s)$. The other population is constituted by wild-type individuals reproducing at rate b . We denote by $x(t)$ the interface between these two populations with $x(0) = x_0$, $x_0 = 1, \dots, N$. If $x(t)$ reaches the absorbing state $x = 0$, then the mutants go extinct. Otherwise, if $x(t)$ reaches the absorbing state $x = N$, the mutants fixate. For simplicity, we neglect inertia. The transition rates for $x(t)$ are expressed by

$$\begin{aligned} r_{x \rightarrow x+1} &= \frac{xb(1+s)}{2}, \\ r_{x \rightarrow x-1} &= \frac{(N-x)b}{2}. \end{aligned} \quad (49)$$

We now assume $N \gg 1$ and approximate $x(t)$ as a continuous process via a Kramers-Moyal expansion. This expansion leads to the Fokker-Plank equation

$$\partial_t P_{x|x_0}(t) = -\partial_x [v(x, t) P_{x|x_0}(t)] + \partial_x^2 [D(x, t) P_{x|x_0}(t)], \quad (50)$$

where the drift and diffusion coefficients are

$$v(x) = \frac{[x(2+s) - N]b}{2}, \quad D(x) = \frac{1}{2} \frac{(N+xs)b}{2}. \quad (51)$$

The probabilities of being absorbed at 0 and N given the initial state x_0 are expressed by

$$\pi_0(x_0) = \frac{\int_0^N \psi(x') dx'}{\int_0^N \psi(x') dx'}, \quad \pi_N(x_0) = \frac{\int_0^l \psi(x') dx'}{\int_0^N \psi(x') dx'}, \quad (52)$$

where

$$\psi(x') = \left(\frac{N+x's}{N} \right)^{\frac{4N(1+s)}{s^2}} \exp\left(-\frac{2(2+s)}{s} x' \right), \quad (53)$$

see [46]. Substituting Eq. (53) into Eq. (52), we obtain Eq. (21).

Appendix: Additional experimental information

1. Bacteria strains and maintenance

MG1655, an *E. coli* strain derived from K-12 wild-type strain, was used in this study as a kind gift from Dr. Paola Laurino at Okinawa Institute of Science and Technology Graduate University. To allow single bacteria tracking in microchannels, a low-copy plasmid harboring the promoter sequence for 30s ribosomal protein and kanamycin resistance (Kan^R) cassette was used to constitutively express green fluorescent protein (pUA66 PrpsL-GFP Kan^R). The pUA66 PrpsL-GFP

was a gift from Dr. Pamela Silver from Harvard University (Addgene plasmid #105606; <http://n2t.net/addgene:105606>; RRID: Addgene_105606) [36]. To visualize both green and red fluorescent markers simultaneously, a pUA66 plasmid harboring rpsL promoter with mCherry open reading frame was constructed by Vector-Builder (vector ID:VB200629-1195vze, vectorbuilder.jp). The plasmid was transformed in MG1655 using standard chemical transformation with ice-cold 0.1 M calcium chloride and 42°C heat shock [47].

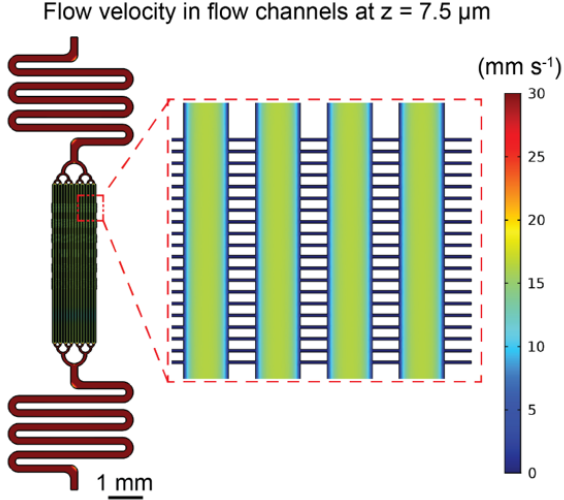


FIG. 12. Numerical simulation of the fluid flow in the PDMS microdevice. The dashed inset in red shows the magnified region in the chip where the flow channels have high flow velocity ($16.2 \pm 0.3 \text{ mm s}^{-1}$).

2. Microfluidic chip simulation and microfabrication

Microfluidic chip numerical simulation. The 3D microchannel design was created by AutoCAD (Autodesk, USA) and exported into COMSOL Multiphysics (COMSOL Inc, USA) with tetrahedral mesh for numerical simulation and microfabrication for numerical simulation and microfabrication. The creeping flow module was used and $10 \text{ mm}^3 \text{ min}^{-1}$ flow rate was set as boundary condition to simulate the culture media flowing in the microfluidic channel. The flow rate distribution in the mid-plane of growth channels was used to optimize the flow equalizing channel design (Fig. 12).

To further characterize the shear flow at the openings of the growth channel, the flow velocity and shear rate at mid plane ($z = 0.5 \mu\text{m}$) of the 3 mm-wide growth channels were analyzed (Fig. 13a). The flow velocity at $\pm 1 \mu\text{m}$ at the openings was $0.28 \pm 0.01 \text{ mm s}^{-1}$ with shear rate of $691.3 \pm 23.8 \text{ (s}^{-1}\text{)}$. The flow velocity in the growth channels, $5 \mu\text{m}$ from the openings was $5.1 \times 10^{-4} \pm 2.1 \times 10^{-5} \text{ (mm s}^{-1}\text{)}$ with shear rate of $0.29 \pm 0.01 \text{ (s}^{-1}\text{)}$ (Fig. 13b and d). This simulation results confirmed the

high shear rate regime at the channel openings to enable the removal of old bacteria while keeping bacteria maintenance in the middle of the growth channels.

Silicon mold microfabrication. Due to the difficulty to align microstructures, a three-step fabrication procedure was taken. First, $5 \mu\text{m}$ -high negative photoresist (mr-DWL-5, Micro Resist Technology GmbH, Germany), was spin-coated on a piece of 4-inch silicon wafer (E&M, Japan) using a spin coater (MS-B150, Mikasa, Japan). An alignment pattern containing cross-shaped microstructures were exposed at 405 nm using a maskless writer (DL-1000, Nanosystems Solutions, Japan). The structures were developed in propylene glycol methyl ether acetate (PGMEA, Sigma-Aldrich, USA) and washed thoroughly with isopropanol and distilled water before dried under nitrogen air.

For the $1 \mu\text{m}$ -high growth channel layer, the mr-DWL-5 photoresist was diluted with gamma butyrolactone (B103608, Sigma-Aldrich, USA) at 7.5:1 (w/w) ratio and spin-coated on the silicon wafer containing alignment microstructures at 7500 rpm for 30s. After appropriate soft bake based on manufacturer's protocol, the patterns for the growth layer channels were exposed using the DL-1000 maskless writer with 2X subpixel exposure followed by a post exposure bake at 95°C for 5 min, finally cooled down to room temperature. Without development of the growth channel layer, the mr-DWL-5 photoresist for the flow channel layer ($15 \mu\text{m}$) was spin-coated on the post exposure-baked mold and soft-baked according to manufacturer's protocol. The flow channel pattern was aligned and exposed using the same maskless writer. After post-exposure hard bake at 95°C for 5 min, the mold was developed in PGMEA solution and washed thoroughly with isopropanol and distilled water before dried under nitrogen air. The true heights of the microstructures were confirmed with a stylus profilometer (Dektak, Bruker, USA).

Fabrication of PDMS microdevices. The fabricated silicon mold was passivated with Trichloro (1H, 1H, 2H, 2H-perfluorooctyl)silane (Sigma-Aldrich, USA) fume in a vacuum desiccator for 2 hours. The passivated mold was placed in a custom mold made in-house with polytetrafluoroethylene for casting 4 mm-high poly(dimethylsiloxane) (PDMS) silicone rubber on the mold. PDMS (Sylgard 184, Dow Corning, USA) was mixed and degassed at 10:1=A:B ratio (Thinky ARE-310, Japan). Appropriate amount of PDMS was poured on the mold and casted with a cover of transparent acrylic sheet at 60°C for at least 4 hours. After PDMS crosslinking, individual piece was diced from the PDMS and 21G holes were punched at the inlet and outlet using a puncher (Accu-punch MP, Syneo, USA). High-precision cover glasses (No.1.5H, $60 \times 24 \times 0.175 \text{ mm}$, Paul Marienfeld GmbH, Germany) were mounted on a 3D-printed washing stand made in-house and ultrasonically washed in 1% TFD4 (Franklab, France) and distilled water before drying in an 80°C oven. Two PDMS pieces were then bonded to a piece of cover glass using plasma sur-

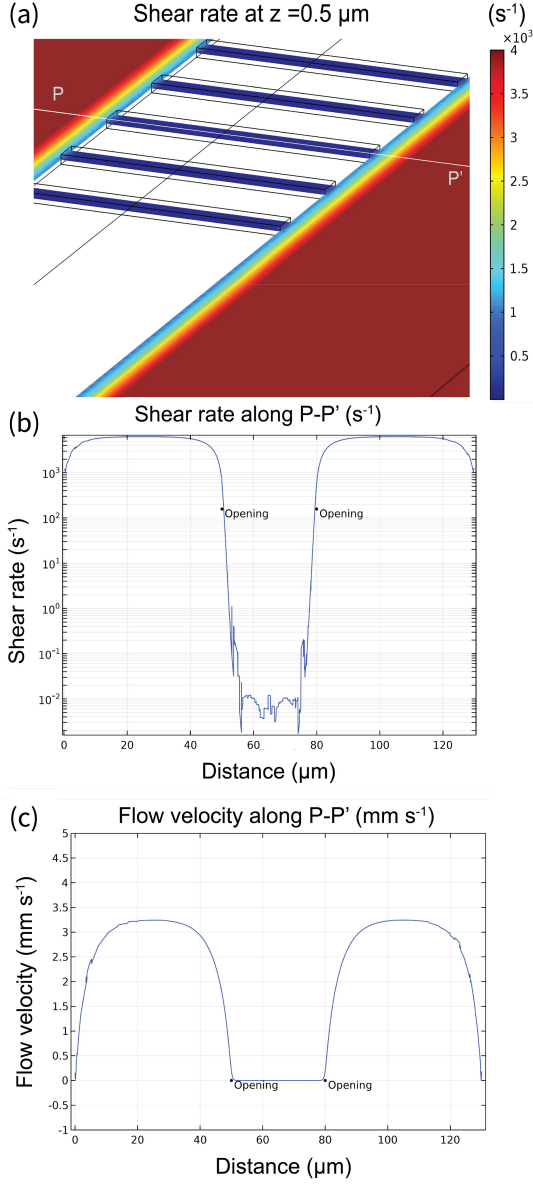


FIG. 13. The numerical simulation of fluid flow at the intersection of flow channels and growth channels. (a) The shear rate at the mid-plane ($z = 0.5 \mu\text{m}$) of growth channel. (b,c) Data from the transverse line along P and P' on the side wall of the flow channels were extracted for quantification.

face activation (PDC-001-HP, Harrick Plasma, USA) at about 10° tilted angle to the long edge of the cover glass to avoid interference by microstructures to the optical focus locking mechanism of the microscope. After bonding, the two PDMS pieces on the cover glass were split using a diamond scribe (Ted Pella, USA). A piece of 2 mm-thick acrylic frame was cut with a CO_2 laser cutter (VLS2.30, Universal Laser Systems, USA) and adhered on the PDMS piece as a reservoir using a dual energy double sided tape (5302A, Nitto, Japan), finishing the PDMS microdevice.

3. Chip culture and time-lapse microscopy

Preparation of microfluidic chip and media. To avoid microbubbles, the microfluidic channel was first passivated with 99.5% ethanol (Nacalai Tesque, Japan), and replaced with ultrapure water (MilliQ, Millipore, USA) [48]. A passivation solution composed of 2 mg mL^{-1} bovine serum albumin (Nacalai Tesque, Japan) and 0.5 mg mL^{-1} salmon sperm DNA (Thermo Fisher Scientific, USA) was incubated in the channel [37]. A set of tubing with stainless tube (New England Small Tube, USA) connected to a 2.5 mL syringe (Terumo, Japan) was inserted in the outlet of the microfluidic chip. The passivation solution was infused in the microchannels by withdrawal with a syringe pump (YSP-202, YMC co., Ltd, Japan) at $2 \mu\text{L min}^{-1}$ for 30 minutes. To prepare the media for studying bacterial lineage, 5X M9 salt stock ($33.9 \text{ g L}^{-1} \text{ Na}_2\text{HPO}_4$; $15 \text{ g L}^{-1} \text{ KH}_2\text{PO}_4$; $2.5 \text{ g L}^{-1} \text{ NaCl}$; $5 \text{ g L}^{-1} \text{ NH}_4\text{Cl}$) was autoclaved and diluted to 1X with supplementation of filter-sterilized MgSO_4 , CaCl_2 , glucose, kanamycin, rifampine and MEM vitamins (M6895, Sigma-Aldrich, USA) to final concentrations of 2 mM, 0.1 mM, 10 mM, 0.1 mM, 1 μM , and 1X, respectively to formulate the M9 media. All chemicals were purchased from Nacalai Tesque Inc. Japan unless specified. The M9 media were loaded into two 25 mL glass syringes (SGE, Australia) and connected to a set of tubing with stainless tubes.

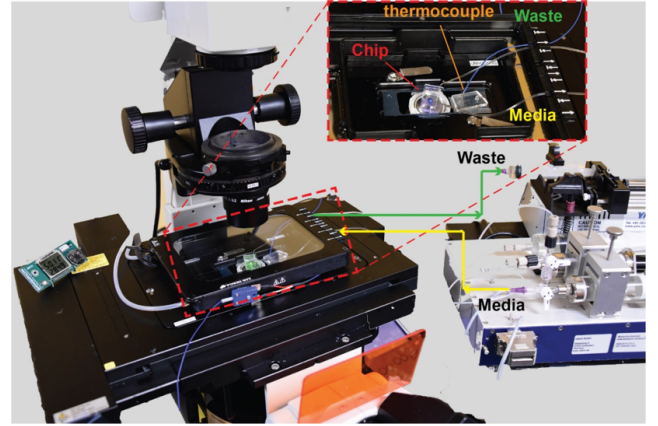


FIG. 14. The photo image of the microscopy setup. The inset shows the PDMS microdevice mounted in the on-stage temperature incubator. The M9 media was infused using a multichannel syringe pump and the waste was withdrawn using a syringe pump at early stage before the flow rate reached $16 \mu\text{L min}^{-1}$ and then left open to atmosphere.

Seeding bacteria on chip and time-lapse microscopy. MG1655 bacteria outgrew overnight in LB broth was inoculated to a new tube of 4 mL LB broth with 0.1 mM kanamycin. The *E. coli* suspension grew at 37°C with 200 rpm shaking until the suspension reached log phase with OD_{600} of 0.2. One mL bacteria suspension was centrifuged at $3000 \times g$ for 10 minutes and resuspended in a 50 microliter (μL) LB broth. The microflu-

idic chip was affixed on a holder in an on-stage incubator (WKSME, Tokai Hit, Japan) on an inverted motorized epi-fluorescence microscope (Ti-E, Nikon, Japan) (see Fig. 14). A dummy microfluidic chip with a K-type thermocouple (ANBE MST Co., Japan) was affixed on the holder for temperature feedback and control. The concentrated *E. coli* suspension was injected in the microchannels using a micropipette and appropriate amount of passivation solution in the reservoir was ensured to equalize the hydrostatic pressure difference between the inlet and the outlet [48]. The bacteria were allowed to swim into the growth channel and to grow for 2 hours at 37°C before the tubing of M9 media infusion was inserted into the inlet and the perfusion was started at 1.6 $\mu\text{L min}^{-1}$ using a multichannel syringe pump (neMESYS, Cetoni GmbH, Germany). The perfusion rate was doubled every 2 hours until it reached 16 $\mu\text{L min}^{-1}$. The microchannels populated by cells were imaged in time-lapse microscopy. For visualization of bacterial population using MG1655 with GFP or mCherry fluorescent proteins, the imaging began after the initial incubation. To start time-lapse microscopy, either an 100X oil immersion objective or a 60X oil immersion objective (Plan apo lambda, Nikon, Japan) with 1.5X intermediate magnification was used to take time-lapse images of the bacteria in the growth channels with focus locking assistance using the Perfect Focus System in the Nikon microscope. The bacteria were tracked using epi-fluorescence imaging using mercury lamp excitation (Intensilight, Nikon, Japan) with GFP or mCherry filter cubes (Semrock, IDEX Corp, USA). The images were taken on a scientific complementary metal oxide semiconductor camera (sCMOS, Prime95B, Photometrics, Canada) at an interval of 3 minutes and exported from the NIS Element software (Nikon, Japan). XY drift due to thermal noise and repeatability of the motorized stage was corrected when necessary using the Stackreg plugin in Fiji ImageJ [10,11].

4. Characterization of bulk bacteria growth

The MG1655 *E. coli* strain with the pUA66 plasmid was cultured in 4 mL LB broth with 0.1 mM kanamycin at 37°C shaken in 200 rpm overnight. 1 μL of the suspensions were inoculated into fresh 1.5 mL LB broth or M9 medium with 10 mM glucose and 1X MEM vitamin, both supplemented with 0.1 mM kanamycin. The suspensions were placed in a 1.6 mL polystyrene cuvette (Sarstedt, Germany) and measured at OD₆₀₀ every minute in a UV spectrometer (UV-1800, Shimadzu, Japan). A temperature control unit was used to keep the cuvette at 37°C. The measurements were performed in triplicate.

The optical density data in early log phase (2-3 hr) of the MG1655 in the two media was fitted to an exponential function $Y_t = Y_0 e^{kt}$, where k was the rate constant, and t was time. The doubling time was calculated by $\ln(2)/k$. The doubling time of MG1655 *E. coli* in LB media was

Bulk growth kinetics of MG1655 pUA66 PrpsL-GFP

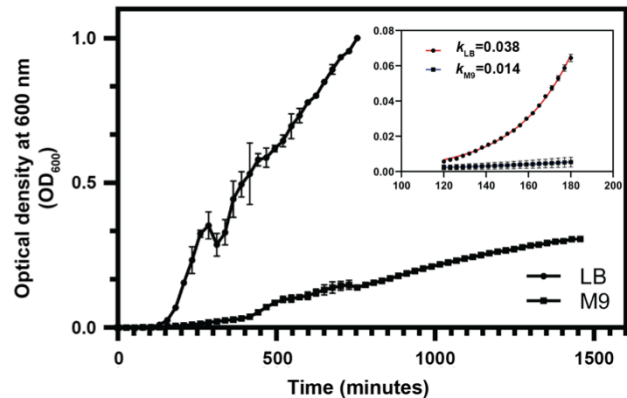


FIG. 15. The growth kinetics of MG1655 with pUA66 PrpsL-GFP plasmid in bulk LB broth or M9 media monitored by optical density at 600 nm (OD₆₀₀) at every minute. The inset shows the early log phase during second and third hour. The growth curve was fitted with exponential growth model to obtain the growth rate constant k . The growth rate constant in LB was 0.038 (min^{-1}), corresponds to a doubling time of 18.1 minutes. The growth rate constant in M9 media was 0.014 (min^{-1}), corresponds to a doubling time of 49.2 minutes.

calculated to be 18.1 minutes and 49.2 minutes in M9 media (Fig. 15).

-
- [1] Z. You, D. J. Pearce, A. Sengupta, and L. Giomi, Geometry and mechanics of microdomains in growing bacterial colonies, *Phys. Rev. X*, **8**, 031065 (2018).
- [2] D. Dell'Arciprete, M. Blow, A. Brown, F. Farrell, J. S. Lintuvuori, A. McVey, D. Marenduzzo, and W. C. Poon, A growing bacterial colony in two dimensions as an active nematic, *Nat. Commun.*, **9**, 1 (2018).
- [3] H. Cho, H. Jönsson, K. Campbell, P. Melke, J. Williams, B. Jedynak, A. Stevens, A. Groisman, and A. Levchenko,

- Self-organization in high-density bacterial colonies: efficient crowd control, *PLoS Biol.*, **5**, e302 (2007).
- [4] B. Karamched, W. Ott, I. Timofeyev, R. Alnahhas, M. Bennett, and K. Josić, Moran model of spatial alignment in microbial colonies, *Physica D*, **395**, 1 (2019).
- [5] J. Sheats, B. Sclavi, M. Lagomarsino, P. Cicuta, and K. Dorfman, Role of growth rate on the orientational alignment of *Escherichia coli* in a slit, *R. Soc. Open Sci.*, **4**, 170463 (2017).

- [6] D. Volfson, S. Cookson, J. Hasty, and L. Tsimring, Biomechanical ordering of dense cell population, *Proc. Natl. Acad. Sci. U.S.A.* **105**, 15346 (2008).
- [7] D. Boyer, W. Mather, O. Mondragón-Palomino, S. Orozco-Fuentes, T. Danino, J. Hasty, and L. Tsimring, Buckling instability in ordered bacterial colonies, *Phys. Biol.* **8**, 026008 (2011).
- [8] K. Coyte, H. Tabuteau, E. Gaffney, K. Foster, and W. Durham, Microbial competition in porous environments can select against rapid biofilm growth, *Proc. Natl. Acad. Sci. U.S.A.* **114**, 161–170 (2016).
- [9] S. M. Janes, S. Lowell, and C. Hutter, Epidermal stem cells, *J. Pathol.* **197**, 479 (2002).
- [10] J. Cairns, Mutation selection and the natural history of cancer, *Nature* **255**, 197 (1975).
- [11] K. Kwapiszewska, R. Kwapiszewski, and Z. Brzózka, Microfluidic devices as tools for mimicking in vivo environment, *New J. Chem.* **35**, 979 (2011).
- [12] R. Rusconi, M. Garren, and R. Stocker, Microfluidics expanding the frontiers of microbial ecology, *Annu. Rev. Biophys.* , 65 (2014).
- [13] J. Männik, R. Driessen, P. Galajda, J. Keymer, and C. Dekker, Bacterial growth and motility in sub-micron constrictions, *Proc. Natl. Acad. Sci. U.S.A.* **106**, 14861 (2009).
- [14] W. Mather, O. Mondragón-Palomino, T. Danino, J. Hasty, and L. Tsimring, Streaming instability in growing cell populations, *Phys. Rev. Lett.* **104**, 208101 (2010).
- [15] P. Wang, L. Robert, J. Pelletier, W. Dang, F. Taddei, A. Wright, and S. Jun, Robust growth of *Escherichia coli*, *Curr. Biol.* **20**, 1099 (2010).
- [16] M. Hashimoto, T. Nozoe, H. Nakaoka, R. Okura, S. Akiyoshi, K. Kaneko, E. Kussell, and Y. Wakamoto, Noise-driven growth rate gain in clonal cellular populations, *Proc. Natl. Acad. Sci. U.S.A.* **113**, 3251 (2016).
- [17] M. Kimura and G. Weiss, The stepping stone model of population structure and the decrease of genetic correlation with distance, *Genetics* **49**, 561 (1964).
- [18] K. Korolev, M. Avlund, O. Hallatschek, and D. Nelson, Genetic demixing and evolution in linear stepping stone models, *Rev. Modern Phys.* **82**, 1691 (2010).
- [19] E. Lieberman, C. Hauert, and M. Nowak, Evolutionary dynamics on graphs, *Nature* **433**, 312 (2005).
- [20] G. Bradburd and P. L. Ralph, Spatial Population Genetics: It’s About Time, *Annu. Rev. Ecol. Evol. Sys.* **50**, 427 (2019).
- [21] M. Nowak, C. Tarnita, and T. Antal, Evolutionary dynamics in structured populations, *Philos. Trans.* **365**, 19 (2010).
- [22] V. Sood, T. Antal, and S. Redner, Voter models on heterogeneous networks, *Phys. Rev. E* **77**, 041121 (2008).
- [23] M. Nowak, F. Michor, and Y. Iwasa, The linear process of somatic evolution, *Proc. Natl. Acad. Sci. U.S.A.* **100**, 14966 (2004).
- [24] B. Allen and M. A. Nowak, Evolutionary shift dynamics on a cycle, *J. Theor. Biol.* **311**, 28 (2012).
- [25] T. Shimaya, T. Takuro, and K. Takeuchi, Lane formation and critical coarsening in a model of bacterial competition, *Phys. Rev. E* **99**, 042403 (2019).
- [26] B. Charlesworth, Fisher, Medawar, Hamilton and the evolution of aging, *Genetics* **156**, 927 (2000).
- [27] M. Imhof and C. Schlötterer, Fitness effects of advantageous mutations in evolving *Escherichia coli* populations, *Proc. Natl. Acad. Sci. U.S.A.* **98**, 1113 (2001).
- [28] M. Kimura, On the probability of fixation of mutant genes in a population, *Genetics* **47**, 713 (1962).
- [29] O. Hallatschek, P. Hersen, S. Ramanathan, and D. R. Nelson, Genetic drift at expanding frontiers promotes gene segregation, *Proc. Natl. Acad. Sci. U.S.A.* **104**, 19926 (2007).
- [30] M. Vishwakarma and E. Piddini, Outcompeting cancer, *Nat. Rev. Cancer* **20**, 1 (2020).
- [31] A. D. Gregorio, S. Bowling, and T. Rodriguez, Cell competition and its role in the regulation of cell fitness from development to cancer, *Dev. Cell* **38**, 621 (2016).
- [32] W. Smith, Y. Davit, J. Osborne, W. Kim, K. Foster, and J. Pitt-Francis, Cell morphology drives spatial patterning in microbial communities, *Proc. Natl. Acad. Sci. U.S.A.* **114**, 201613007 (2016).
- [33] J. Kayser, C. Schreck, Q. Yu, M. Gralka, and O. Hallatschek, Emergence of evolutionary driving forces in pattern-forming microbial populations, *Philos. Trans. R Soc. Lond. B Biol. Sci.* **373**, 20170106 (2018).
- [34] M. Delarue, J. Hartung, C. Schreck, P. Gniewek, L. Hu, S. Herminghaus, and O. Hallatschek, Self-driven jamming in growing microbial populations, *Nat. Phys.* **12**, 762 (2016).
- [35] D. Bi, X. Yang, M. C. Marchetti, and M. L. Manning, Motility-driven glass and jamming transitions in biological tissues, *Phys. Rev. X* **6**, 021011 (2016).
- [36] F. Stirling, L. Bitzan, S. O’Keefe, E. Redfield, J. Oliver, J. Way, and P. Silver, Rational design of evolutionarily stable microbial kill switches, *Mol. Cell* **68**, 686 (2017).
- [37] M. Kaiser, F. Jug, T. Julou, S. Deshpande, T. Pfohl, O. Silander, and E. Nimwegen, Monitoring single-cell gene regulation under dynamically controllable conditions with integrated microfluidics and software, *Nat. Commun.* **9**, 212 (2018).
- [38] L. Saias, J. Autebert, L. Malaquin, and J. Viovy, Design, modeling and characterization of microfluidic architectures for high flow rate, small footprint microfluidic systems, *Lab Chip* **11**, 822 (2011).
- [39] D. Qin, Y. Xia, and G. Whitesides, Soft lithography for micro-and nanoscale patterning, *Nat. Protoc.* **5**, 491 (2010).
- [40] R. Funari, N. Bhalla, K. Y. Chu, B. Söderström, and A. Q. Shen, Nanoplasmonics for real-time and label-free monitoring of microbial biofilm formation, *ACS Sens.* **3**, 1499–1509 (2018).
- [41] C. Schneider, W. Rasband, and K. Eliceiri, NIH Image to ImageJ: 25 years of image analysis, *Nat. Methods* **9**, 671–675 (2012).
- [42] P. Thévenaz, U. Ruttimann, and M. Unser, A pyramid approach to subpixel registration based on intensity, *IEEE Trans. Image Process.* **7**, 27 (1998).
- [43] A. Ducret, E. M. Quardokus, and Y. V. Brun, MicrobeJ, a tool for high throughput bacterial cell detection and quantitative analysis, *Nat. Microbiol.* **1**, 16077 (2016).
- [44] K. Thirusittampalam, M. J. Hossain, O. Ghita, and P. Whelan, A novel framework for cellular tracking and mitosis detection in dense phase contrast microscopy images, *IEEE J Biomed. Health* **17**, 642 (2013).
- [45] R. Usmani, Inversion of Jacobi’s tridiagonal matrix, *Comput. Math.* **27**, 59–66 (1994).
- [46] C. Gardiner, *Stochastic Methods: A Handbook for the Natural and Social Sciences*, Springer Series in Synergetics (Springer Berlin Heidelberg, 2009).
- [47] J. Sambrook and D. W. Russell, Preparation and trans-

formation of competent *E. coli* using calcium chloride, Cold. Spring. Harb. Protoc. 2006; 2006:pdb.prot3932 **1** (2006).

[48] H.-F. Tsai, C. IJspeert, and A. Q. Shen, Voltage-gated

ion channels mediate the electrotaxis of glioblastoma cells in a hybrid pmma/pdms microdevice, APL Bioeng. **4**, 036102 (2020).